

# Mott Transitions and $d$ -wave Superconductivity in Half-Filled-Band Hubbard Model on Square Lattice with Geometric Frustration

Hisatoshi YOKOYAMA,\* Masao OGATA<sup>1</sup> and Yukio TANAKA<sup>2</sup>

*Department of Physics, Tohoku University, Sendai 980-8578*

<sup>1</sup>*Department of Physics, University of Tokyo, Bunkyo-ku, Tokyo 113-0033*

<sup>2</sup>*Department of Applied Physics, Nagoya University, Nagoya 464-8603*

Mechanisms of Mott transitions and  $d_{x^2-y^2}$ -wave superconductivity (SC) are studied in the half-filled-band Hubbard model on square lattices with a diagonal hopping term ( $t'$ ), using an optimization (or correlated) variational Monte Carlo method. In the trial wave functions, a doublon-holon binding effect is introduced in addition to the onsite Gutzwiller projection. We mainly treat a  $d$ -wave singlet state and a projected Fermi sea. In both wave functions, first-order Mott transitions without direct relevance to magnetic orders take place at  $U = U_c$  approximately of the bandwidth for arbitrary  $t'/t$ . These transitions originate in the binding or unbinding of a doublon to a holon.  $d$ -wave SC appears in a narrow range immediately below  $U_c$ . The robust  $d$ -wave superconducting correlation are necessarily accompanied by enhanced antiferromagnetic correlation; the strength of SC becomes weak, as  $t'/t$  increases.

KEYWORDS: Mott transition, superconductivity, condensation energy, antiferromagnetic correlation, spin gap, high- $T_c$  cuprate, Hubbard model, variational Monte Carlo method, frustration

## 1. Introduction

In connection with the superconductor-insulator transitions in organic compounds  $\kappa$ -(BEDT-TTF)X,<sup>1</sup> the half-filled-band Hubbard model on anisotropic triangular lattices [Fig. 1(b)]<sup>2</sup> have been intensively studied. In addition, a recent experimental study<sup>3</sup> have reported that a series of film samples of non-doped high- $T_c$  cuprates (parent materials of electron-doped systems) do not become antiferromagnetic (AF) insulators but exhibit metallic properties including superconductivity (SC) at 21K. Thus, it is important to grasp the mechanisms of Mott transitions and SC, if any, in half-filled-band Hubbard models with frustration. Because such phenomena arise at intermediate correlation strength ( $U \sim W$ ;  $W$  being the bandwidth), one has to use a method which can reliably treat both strongly-correlated and weakly-correlated regimes. As one of such methods, the optimization (or correlated) variational Monte Carlo (VMC) method<sup>4</sup> has rapidly progressed in recent years to study ground-state properties.<sup>5</sup>

Using this method, the present authors have recently studied the Hubbard model on the anisotropic triangular lattice [Fig. 1(b)].<sup>6</sup> With a projected  $d$ -wave singlet state, it is found that (1) a conductive-to-nonmagnetic-insulator (Mott) transition takes place at  $U = U_c$ , which is somewhat smaller than  $W$ , and is caused by the binding (and unbinding) of a doublon to a holon; (2)  $d_{x^2-y^2}$ -wave SC appears in the vicinity of both the Mott transition and the AF phase, and develops together with the short-range AF correlation (or fluctuation).

In weakly frustrated cases, the two lattices Fig. 1(a) and (b) have a common characteristic wave number  $\mathbf{G} = (\pi, \pi)$  in spin correlation. In strongly frustrated cases, however, the characteristic wave numbers become different; for instance, 120-degree-structure spin corre-

lation will be dominant in (b) for  $t' \sim t$ ,<sup>7</sup> whereas the so-called collinear structure will be favored in (a). In this paper, we carry out similar detailed calculations for the lattice often treated in the context of high- $T_c$  cuprates ( $t$ - $t'$ - $U$  model) [Fig. 1(a)], and reveal whether or not the above mechanisms of the Mott transition and of SC also work here. In addition to the  $d$ -wave singlet state, we study Mott transitions in the projected Fermi sea.

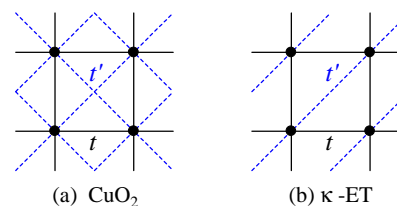


Fig. 1. (Color online) Lattice structure and hopping integrals  $t$  and  $t'$ , (a) studied in this work, and (b) often used for  $\kappa$ -BEDT-TTF salts. Lattice sites are denoted by dots.

The organization of this paper is as follows: In §2, we introduce the model and method we deal with. In §3 and §4, we discuss Mott transitions in the  $d$ -wave singlet state and in the projected Fermi sea, respectively. Section 5 is assigned to the stability and properties of the  $d$ -wave superconducting (SC) state. In §6, we construct a ground-state phase diagram based on the present VMC calculations, and address important problems with respect to antiferromagnetism (AF). In §7, we briefly summarize the main results and give some further discussions.

Part of the present results has been reported in a previous letter.<sup>8</sup>

## 2. Model and Method

In §2.1, the model we study is introduced, and related studies are mentioned in short. In §2.2, we briefly review the background of variational wave functions for the

\*E-mail: yoko@cmpt.phys.tohoku.ac.jp

Hubbard model in the research on the Mott transition. In §2.3, we give an account of the wave functions used in this paper and the conditions of VMC calculations.

### 2.1 Hubbard model on frustrated square lattices

In this paper, we study the Hubbard model<sup>9–11</sup> on a square lattice with diagonal transfer  $t'$  [Fig. 1(a)],

$$\mathcal{H} = \mathcal{H}_{\text{kin}} + \mathcal{H}_U = \sum_{\mathbf{k}\sigma} \varepsilon(\mathbf{k}) c_{\mathbf{k}\sigma}^\dagger c_{\mathbf{k}\sigma} + U \sum_j n_{j\uparrow} n_{j\downarrow}, \quad (1)$$

$$\varepsilon(\mathbf{k}) = -2t(\cos k_x + \cos k_y) - 4t' \cos k_x \cos k_y, \quad (2)$$

with  $U, t > 0$ . This model eq. (1) has been often used as a simple model which probably captures the essence of cuprates.<sup>12</sup> Here, we concentrate on the half-filled band ( $n = N_e/N_s = 1$ ;  $N_e$ : electron number and  $N_s$ : site number) and leave doped cases for a forthcoming publication. We exclusively treat the cases of  $t' \leq 0$ , because the behavior for  $t' (> 0)$  is identical to that for  $-t'$ , due to the particle-hole symmetry at  $n = 1$ . Note that the negative sign of  $t'/t$  agrees with the hole-doped case of high- $T_c$  cuprates. When  $|t'/t|$  is varied, the features of the bare band eq. (2) abruptly change at  $|t'/t| = 0.5$ , where low-lying energy levels become enormously degenerate; the van Hove singularity points depart from  $(\pi, 0)$  and  $(0, \pi)$  for  $|t'/t| > 0.5$ . Furthermore, the plausible values of high- $T_c$  cuprates are considered as  $|t'/t| = 0.1$ – $0.3$ .<sup>13</sup> Thus, we restrict the range of frustration strength to  $0 \leq |t'/t| \leq 0.5$  in this paper.

Despite the importance of the model, reliable knowledge is limited particularly in the intermediate and strong coupling regimes. For the pure square lattice ( $t' = 0$ ), it is believed that the ground state is insulating with a long-range AF order for  $U > 0$ , due to the complete nesting condition.<sup>14</sup> For frustrated cases ( $t' \neq 0$ ), however, it is a present vital problem to clarify the properties of the conductor-insulator transition.<sup>15–18</sup> As for SC at half filling, although the anisotropic triangular lattices has been often taken up,<sup>19</sup> studies on the present lattice seem rare to our knowledge.

### 2.2 Historical background of wave functions

As a many-body trial wave function, the Jastrow type<sup>20</sup> is useful and has been often used:  $\Psi = \mathcal{P}\Phi$ , where  $\mathcal{P}$  denotes a many-body correlation (Jastrow) factor composed of projection operators, and  $\Phi$  a one-body wave function usually given by a Slater determinant. For the Hubbard model, more than four decades ago, Gutzwiller introduced the celebrated onsite projection,<sup>11</sup>

$$\mathcal{P}_G = \prod_j [1 - (1 - g)n_{j\uparrow}n_{j\downarrow}], \quad (3)$$

which has primary importance for arbitrary parameters in the Hubbard model. Although the Gutzwiller wave function (GWF),  $\Psi_G^{\text{FS}} = \mathcal{P}_G \Phi_F$  ( $\Phi_F$ : Fermi sea), looks simple, it is generally difficult to accurately calculate expectation values with it. Hence, a mean-field-type approximation [now called Gutzwiller approximation (GA)] was introduced by Gutzwiller himself,<sup>21</sup> and had been used and extended by many researchers for the next two decades.<sup>22</sup> However, the variation theory loses its various

advantages when additional approximations like GA is applied, and consequently it becomes difficult to improve the wave function. To break this deadlock, VMC methods<sup>23</sup> have been applied to this problem;<sup>24,25</sup> thereby, and by subsequent exact analytic treatment in one dimension,<sup>26</sup> the precise behavior of  $\Psi_G^{\text{FS}}$  was clarified for the first time. Although  $\mathcal{P}_G$  is indispensable to treat the Hubbard model, its independent use leads to the following physically unsatisfactory results: (1) The momentum distribution function  $n(\mathbf{k})$  tends to be an increasing function of  $|\mathbf{k}|$ , (2)  $2k_F$  anomalies in the spin [charge density] structure factor  $S(\mathbf{q})$  [ $N(\mathbf{q})$ ] cannot be properly represented, and (3) a Mott transition cannot be described, in addition to a sizably high variational energy.

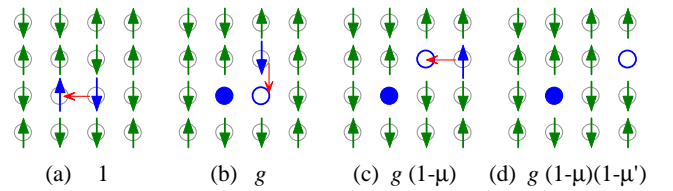


Fig. 2. (Color online) Weight assignment of the Jastrow factor  $\mathcal{P} = \mathcal{P}_Q \mathcal{P}_G$  depending on the local electron configuration. A solid (open) blue circle indicates a doublon (holon). Red thin arrows denote virtual hopping processes in the strong-coupling expansion. (a) A configuration with no doublon; a basis for  $U/t \rightarrow \infty$ . (b) A doublon sits at a nearest neighbor of a holon; a virtual state in the second order of strong-coupling expansion in  $t/U$ . (c) A doublon sits at a diagonal neighbor of a holon; a virtual state in the second (fourth) order in  $t'/U$  ( $t/U$ ). (d) A doublon sits at a farther site of a holon; a higher-order virtual state. For the case of eq. (4), we should place  $\mu' = 0$ .

Although the electron-electron interaction in the Hubbard model is limited within a single site, its effect reaches distant sites. Therefore, to overcome the above shortcomings of  $\mathcal{P}_G$ , one needs to add intersite correlation (long-range Jastrow) factors. In cases of low electron density, distance-dependent long-range Jastrow factors are useful.<sup>27</sup> On the other hand, at half filling, short-range part of the Jastrow factor will be dominant due to the screening effect. Castellani *et al.*<sup>28</sup> derived an effective Hamiltonian of the Hubbard model, taking account of both spin and charge degrees of freedom. In their effective Hamiltonian, there appears an exchange term between a doubly occupied site (doublon) and an empty site (holon), indicating a doublon-holon correlation is inherent in the Hubbard model. Kaplan *et al.*<sup>29</sup> actually showed by studying one-dimensional (1D) small clusters that the binding of a doublon to a holon is important for large  $U/t$  to reduce the energy at half filling. Using exact diagonalization, Yokoyama and Shiba<sup>27</sup> studied the ground-state wave function of Hubbard rings at half filling, where the ground state is known to be insulating for  $U/t > 0$ .<sup>30</sup> They found that, for large  $U/t$ , the magnitude of coefficients of bases with one doublon (and one holon) decreases exponentially as a function of the distance between the doublon and holon. This means that a doublon is bound to a holon within the decay distance in an insulating state.

A simplified wave function which reflects the above arguments is written as  $\Psi_Q = \mathcal{P}_Q \mathcal{P}_G \Phi$ .<sup>27,29</sup> Here, the doublon-holon binding factor  $\mathcal{P}_Q$  is limited to the nearest-neighbor part:

$$\mathcal{P}_Q = \prod_i (1 - \mu Q_i^\tau), \quad (4)$$

$$Q_i^\tau = \prod_\tau [d_i(1 - e_{i+\tau}) + e_i(1 - d_{i+\tau})], \quad (5)$$

where  $d_i = n_{i\uparrow}n_{i\downarrow}$ ,  $e_i = (1 - n_{i\uparrow})(1 - n_{i\downarrow})$ , and  $\tau$  runs over all the nearest neighbors. A variational parameter  $\mu$  ( $0 \leq \mu \leq 1$ ) controls the strength of doublon-holon binding in the nearest-neighbor sites; as  $\mu$  increases, a doublon tends to adhere to a holon, and for  $\mu \rightarrow 1$ , a doublon cannot leave a holon, as illustrated in Fig. 2.

This Jastrow factor,  $\mathcal{P}_Q \mathcal{P}_G$ , can be derived also naturally from the strong-coupling expansion. It is known that GWF with  $g = 0$  is an extremely good trial state for the 1D Heisenberg model,<sup>25,31</sup> and the Gutzwiller-type functions,  $\mathcal{P}_G \Phi_{\text{AF}}$  and  $\mathcal{P}_G \Phi_{\text{BCS}}$  ( $\Phi_{\text{AF}}$ : Hartree-Fock-type AF state;  $\Phi_{\text{BCS}}$ :  $d_{x^2-y^2}$ -wave BCS state), yield quantitatively reasonable results for the 2D  $t$ - $J$  model.<sup>32-34</sup> These favorable properties of GWF for the strong coupling models can be applied to the Hubbard model by considering a canonical transformation,  $\mathcal{H}_{t-J} \sim e^{iS} \mathcal{H}_{\text{Hub}} e^{-iS}$  ( $t/U \rightarrow 0$ ),<sup>35</sup> and similarly,

$$\frac{\langle \Psi_G | \mathcal{H}_{t-J} | \Psi_G \rangle}{\langle \Psi_G | \Psi_G \rangle} \sim \frac{\langle \Psi_G e^{iS} | \mathcal{H}_{\text{Hub}} | e^{-iS} \Psi_G \rangle}{\langle \Psi_G e^{iS} | e^{-iS} \Psi_G \rangle}. \quad (6)$$

Thus, a wave function improved for the Hubbard model is given by applying the strong coupling expansion,  $e^{-iS}$ , to a Gutzwiller-type function  $\Psi_G$  ( $= \mathcal{P}_G \Phi$ ). Considering virtual hopping processes in this expansion as illustrated in Fig. 2, one easily notice that the first-order terms of this expansion roughly correspond to  $\mathcal{P}_Q \Psi_G$ . In addition, it was found that a more direct form of  $e^{-iS} \Psi_G$  yields improved results<sup>36</sup> similar to those of  $\mathcal{P}_Q \Psi_G$ , mentioned in the following sections.

In the early VMC study of the projected Fermi sea,  $\Psi_Q^{\text{FS}} = \mathcal{P}_Q \mathcal{P}_G \Phi_{\text{F}}$ , for the 1D and 2D square lattices, Yokoyama and Shiba<sup>27</sup> concluded that  $\Psi_Q^{\text{FS}}$  corrects the shortcomings of GWF (1) and (2) mentioned above, but a Mott transition does not arise even in  $\Psi_Q^{\text{FS}}$ . Subsequently, Millis and Coppersmith<sup>37</sup> also derived a conclusion, by calculating a zero-frequency part of the optical conductivity using a VMC technique, that a Mott transition cannot be described within this type of wave functions. However, as we have repeatedly explained in previous papers,<sup>6,38</sup> these early studies were not sufficient and not careful enough to arrive at the correct conclusion that the doublon-holon binding factor  $\mathcal{P}_Q$  is essential to describe a Mott transition. Actually, the existence of Mott transitions has been confirmed using  $\mathcal{P}_Q$  for various systems,<sup>39</sup> such as the square lattice,<sup>8,38</sup> the anisotropic triangular lattice,<sup>6</sup> the kagomé lattice,<sup>40</sup> the checker-board lattice,<sup>41</sup> and a degenerate Hubbard model on the square lattice.<sup>42</sup>

### 2.3 Wave functions and VMC conditions

In this paper, we continue to study the Mott transition induced by  $\mathcal{P}_Q$ . Considering the lattice structure we treat [Fig. 1(a)], we introduce into  $\mathcal{P}_Q$  the effect of doublon-holon binding between diagonal-neighbor sites  $\mu'$  [ $\mathbf{r} = (\pm x, \pm y)$ ], in addition to that of the nearest neighbors,  $\mu$  [ $\mathbf{r} = (\pm x, 0)$  and  $(0, \pm y)$ ]:

$$\mathcal{P}_Q = \prod_i (1 - \mu Q_i^\tau) (1 - \mu' Q_i^{\tau'}), \quad (7)$$

$$Q_i^{\tau(\tau')} = \prod_{\tau(\tau')} [d_i(1 - e_{i+\tau(\tau')}) + e_i(1 - d_{i+\tau(\tau')})], \quad (8)$$

in which  $\tau$  ( $\tau'$ ) runs over all the adjacent sites in the bond directions of  $t$  ( $t'$ ). The weight assignment of the correlation factors  $\mathcal{P} = \mathcal{P}_Q \mathcal{P}_G$  is explained in Fig. 2. For the pure square lattice ( $t' = 0$ ), we use eq. (4) instead of eq. (7) for simplicity, because we could confirm that the effect of  $\mu'$  is negligible even quantitatively for  $t' = 0$ . Anyway, the wave function we deal with in this paper is

$$\Psi_Q = \mathcal{P}_Q \mathcal{P}_G \Phi. \quad (9)$$

As a one-body part  $\Phi$ , we primarily study a fixed-density BCS state:<sup>43</sup>

$$\Phi_d = \left( \sum_{\mathbf{k}} a_{\mathbf{k}} c_{\mathbf{k}\uparrow}^\dagger c_{-\mathbf{k}\downarrow}^\dagger \right)^{\frac{N_e}{2}} |0\rangle, \quad (10)$$

$$a_{\mathbf{k}} = \frac{v_{\mathbf{k}}}{u_{\mathbf{k}}} = \frac{\Delta_{\mathbf{k}}}{\varepsilon_{\mathbf{k}} - \zeta + \sqrt{(\varepsilon_{\mathbf{k}} - \zeta)^2 + \Delta_{\mathbf{k}}^2}}, \quad (11)$$

in which  $\zeta$  is a variational parameter which is reduced to the chemical potential for  $U/t \rightarrow 0$ . Since we know that, at half filling, the simple  $d_{x^2-y^2}$ -wave is the most stable among various gap shapes,<sup>32,33,44</sup> here we exclusively treat the  $d$ -wave gap:

$$\Delta_{\mathbf{k}} = \Delta_d (\cos k_x - \cos k_y). \quad (12)$$

We should emphasize that, although a variational parameter  $\Delta_d$  indicates the magnitude of the  $d$ -wave gap, a state ( $\Psi_Q^d = \mathcal{P} \Phi_d$ ) with finite  $\Delta_d$  does not necessarily mean a SC state.<sup>45</sup> We fix the value of  $t'$  in  $\varepsilon_{\mathbf{k}}$  in the wave functions [eq. (11)] at the same value as that in the Hamiltonian, because the renormalization of  $\varepsilon_{\mathbf{k}}$ <sup>46</sup> is not serious as far as the system is conductive,<sup>6</sup> and  $\zeta$  compensates this effect to some extent in the insulating regime, as we will see later. For  $\Delta_d = 0$ ,  $\Phi_d$  is reduced to  $\Phi_{\text{F}}$  explained next.

As a reference state, we also study the Fermi sea,

$$\Phi_{\text{F}} = \prod_{k < k_{\text{F}}, \sigma} c_{\mathbf{k}\sigma}^\dagger |0\rangle. \quad (13)$$

A complicated point is that  $\Psi_Q^{\text{FS}}$  ( $= \mathcal{P}_Q \mathcal{P}_G \Phi_{\text{FS}}$ ) does not merely represent a normal state;  $\Psi_Q^{\text{FS}}$  also undergoes a Mott transition, as we found for the attractive Hubbard model.<sup>38</sup> The results of the attractive model for the symmetric case ( $t' = 0$  and  $n = 1$ ) are exactly mapped to those of the repulsive model through a canonical transformation.<sup>47</sup> As extension, in this paper, we study the properties of  $\Psi_Q^{\text{FS}}$  for asymmetric cases ( $t' \neq 0$ ).

For comparison in §5 and §6, we take up an ordinary mean-field solution  $\Phi_{\text{AF}}^{48}$  for a one-body AF state with a long-range order. In the trial AF state,

$$\Psi_Q^{\text{AF}} = \mathcal{P}_Q \mathcal{P}_G \Phi_{\text{AF}}, \quad (14)$$

the AF gap  $\Delta_{\text{AF}}$  is optimized as a parameter, but  $t'$  in  $\epsilon_{\mathbf{k}}$  is fixed at the model value, similarly to in  $\Psi_Q^d$ .

Because our trial functions have at most five parameters to be optimized [ $g$ ,  $\mu$ ,  $\mu'$ ,  $\Delta_{d(\text{AF})}$ ,  $\zeta$ ], we have used a simple version of optimization VMC procedures,<sup>49</sup> namely a line minimization of one parameter with the others fixed.<sup>50</sup> In a round of iteration, every parameter is once optimized. In most cases of optimization in this study, the parameters converge within a few rounds, after which we continue the optimization process for more 15-20 rounds. The optimized values of the parameters and energy are determined by averaging the results of these rounds after convergence. Because each optimization procedure is carried out with  $10^5$  (for  $L = 18$ )- $10^6$  (for  $L = 6$ ) samples, preserving the acceptance ratio 0.5, our data are substantially the averages of several million samples. Thereby, the accuracy in the total energy is markedly increased, typically to the order of  $10^{-4}t$ . Because the convergence of optimization becomes very slow near phase transitions, especially continuous-type ones, we have carried out sufficient iteration ( $\sim 50$  rounds) in such cases. With the optimized parameters thus determined, physical quantities are calculated in different VMC jobs with  $1.5\text{-}2.5 \times 10^5$  samples. We used lattices of  $L \times L$  sites ( $L = 6\text{-}18$ , mainly 10-14) with the periodic-antiperiodic boundary conditions. Because the closed-shell condition cannot be satisfied in a wide range of asymmetric model parameters ( $t' \neq 0$ ) at half filling, we are often obliged to calculate with open shells.

Finally, we mention the finite-size analysis in the model eq. (1). For the symmetric case ( $t' = 0$ ), the system-size dependence of various quantities is often monotonic, because the  $\mathbf{k}$ -point structure included in the Fermi surface is systematic with increasing  $L$ . In contrast, in the asymmetric cases, the  $\mathbf{k}$ -point structure is unique to each system size  $L$  and frustration strength  $t'$ ; therefore the system-size dependence becomes irregular, and the  $t'/t$  dependence not smooth.

### 3. Mott Transitions in $d$ -wave State

In this section, we study Mott transitions arising in the  $d$ -wave singlet state  $\Psi_Q^d$ . In §3.1, we show that a first-order transition occurs by observing hysteresis in the  $U/t$  dependence of total energy. In §3.2, we identify this critical behavior as a Mott transition without relevance to magnetic orders, by studying various quantities. In §3.3, we consider the properties of this transition with reference to other studies.

#### 3.1 Total energy and hysteresis behavior

First, let us consider the behavior of the optimized total energy per site,  $E$ . In the inset of Fig. 3,  $E/t$  for  $t'/t = 0$  are plotted for a wide range of  $U/t$  and four system sizes ( $L$ ). In this scale,  $L$  dependence is imperceptible. One readily notices the cusp behavior at  $U/t \sim 6.5$ , where the data points of  $L = 16$  (red) are concentrated.

In the main panel of Fig. 3, this cusp part is magnified. We have optimized the wave function successively, from both weak- and strong-correlation sides toward this cusp point. For the system of  $L = 10$ , the optimized energies from the two sides coincide, and  $E/t$  becomes a smooth function of  $U/t$ . On the other hand, for larger systems ( $L \geq 12$  in Fig. 3), the optimized values in the weak-correlation side are not smoothly connected to those in the strong-correlation side, and vice versa.<sup>51</sup> At these cusp points, all optimized variational parameters have discontinuities, as shown in Fig. 4(a)-(e). Such hysteresis and discontinuities indicate that a first-order phase transition takes place at the cusp point ( $U = U_c$ ). In the following subsection, we identify this transition as a Mott (conductor-to-nonmagnetic-insulator) transition.

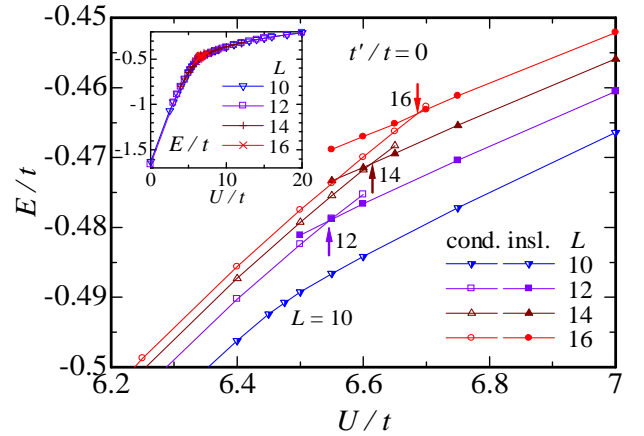


Fig. 3. (Color online) Total energies of the  $d$ -wave state for the pure square lattice ( $t' = 0$ ) for four system sizes near the critical points ( $U_c$ ), indicated by arrows. The behavior of hysteresis is found for  $L = 12\text{-}16$ ; the local minima for the conductive (insulating) sides are denoted by open (solid) symbols. For  $L = 10$ , hysteresis is not found with the present VMC calculations, and the parameters vary continuously. The critical values read  $U_c/t = 6.54, 6.61$  and  $6.69$  for  $L = 12, 14$  and  $16$ , respectively. Inset: The behavior of  $E/t$  for a wider range of  $U/t$ .

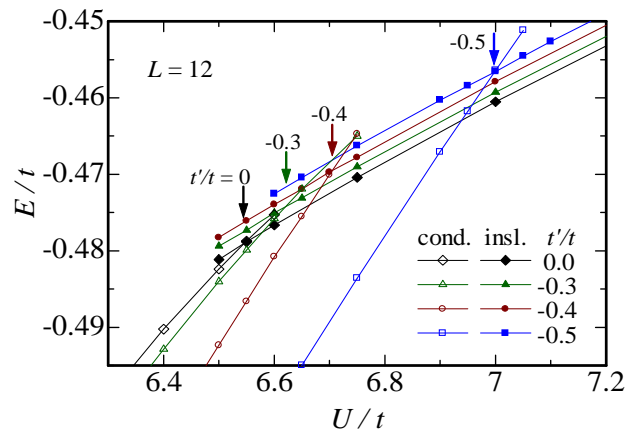


Fig. 5. (Color online) Total energies for four values of  $t'/t$  near the critical points indicated by arrows. The system size is fixed at  $L = 12$ . Hysteresis is found for each case. The local minima for the conductive (insulating) sides are shown by open (solid) symbols. The critical values read  $U_c/t = 6.54, 6.62, 6.70$  and  $7.00$  for  $t'/t = 0, -0.3, -0.4$  and  $-0.5$ , respectively.

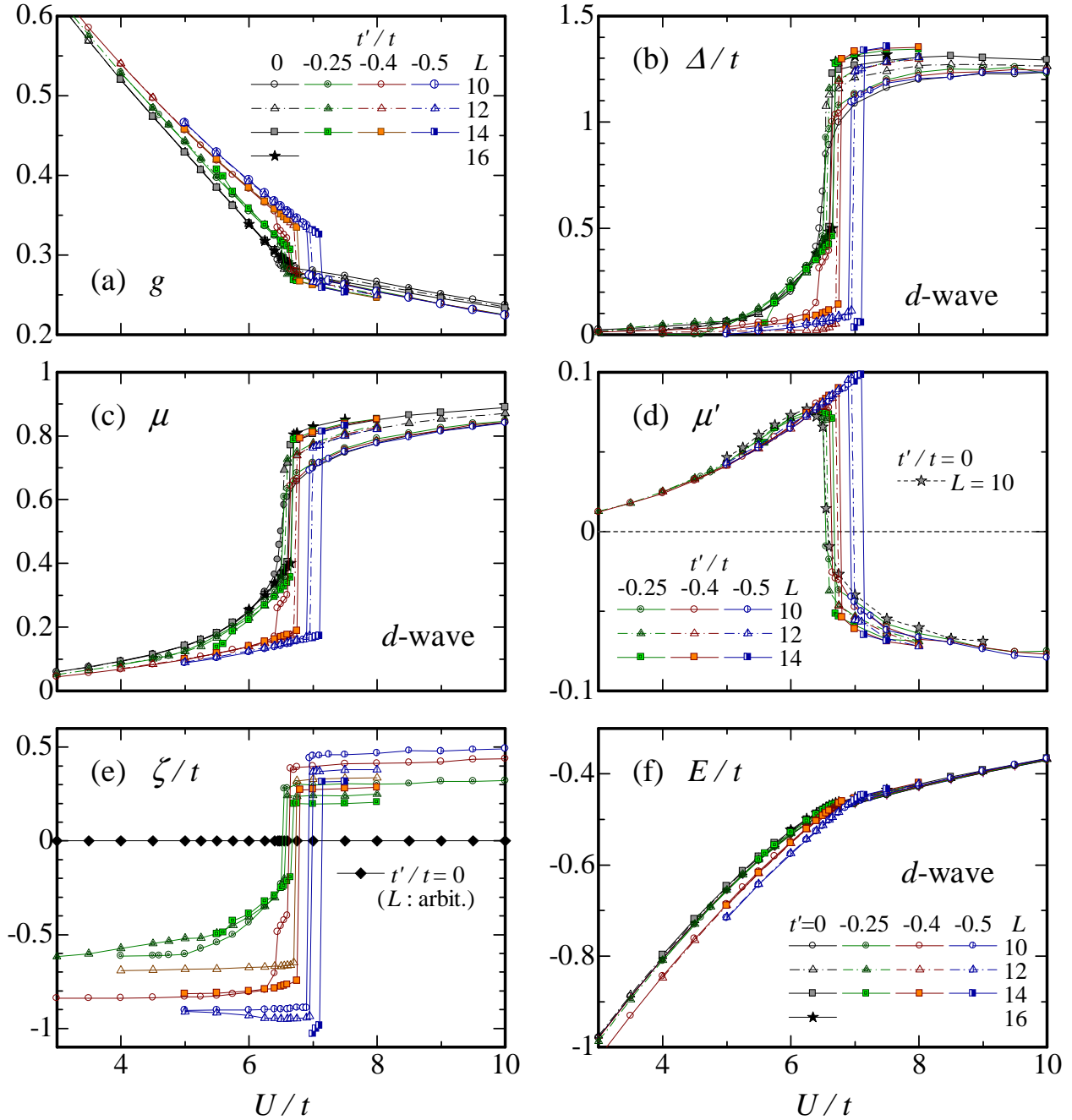


Fig. 4. (Color online) (a)-(e) Optimized variational parameters (at the global minima of  $E/t$ ) for the  $d$ -wave state near the critical values  $U_c$  as a function of  $U/t$ : (a) Onsite correlation (Gutzwiller) factor. (b)  $d$ -wave gap parameter. (c) Doublon-holon binding factor between the nearest-neighbor sites. (d) The same factor between the diagonal-neighbor sites. (e) Chemical potential. For  $t' = 0$ ,  $\zeta$  is always zero due to the band symmetry. (f) Total energies for four values of  $t'/t$ . The symbols and the scales in abscissa are common to all the panels. Data for four values of  $t'/t$ , and for three or four system sizes ( $L \times L$ ) are compared.

Next, we study the  $L$  dependence of the critical point. We first note that it is indispensable to check the system-size dependence when we treat critical phenomena, as we have learned from the distinct behavior between  $L = 10$  and  $L \geq 12$  in Fig. 3. As the system size increases ( $L \geq 12$ ), the critical point shifts to a larger value of  $U/t$  (Fig. 3). This is partly because a large system size is more advantageous to conductive states, which have longer correlation lengths. For  $t'/t = 0$ , because the system-size dependence of  $E/t$  is fitted well with quadratic curves of  $1/N_s$ , the critical value for  $L = \infty$  can be estimated as  $U_c/t = 7.0 \pm 0.1$  using the method of least squares.

Here, we consider the  $t'/t$  dependence. As shown in Fig. 4(f), the total energy  $E/t$  has a cusp also for finite  $t'/t$ . The behavior of  $E/t$  near the cusps is magnified in Fig. 5 for four values of  $t'/t$  and for  $L = 12$ . For  $U < U_c$ ,  $E/t$  is greatly reduced as  $|t'/t|$  increases; this behavior is common to the noninteracting case, in which the gain in  $E_{t'}$  exceeds the loss in  $E_t$  [ $E_t(E_{t'})$ : the contribution from the  $t$  ( $t'$ ) term to  $\langle \mathcal{H}_{\text{kin}} \rangle$ ]. In contrast, for  $U > U_c$ ,  $E/t$  changes only very slightly; we will return to this point in §3.3. Consequently, as  $|t'/t|$  increases, the transition point shifts to a larger value of  $U/t$ , especially rapidly for large  $t'/t$ , although the bandwidth remains constant,  $8t$ ,

for  $0 \leq t'/t \leq 0.5$ . This  $t'/t$  dependence of  $U_c/t$  can be checked in the behavior of the parameters [Figs. 4(a)-(e)].

In Fig. 6, we show the system-size dependence of  $E/t$  near  $U_c/t$  for strongly frustrated cases ( $t'/t = -0.4$  and  $-0.5$ ). Here, even the system as small as  $L = 10$  exhibits clear hysteresis. The critical value  $U_c/t$  tends to increase monotonically, as  $L$  increases, although the extrapolation of  $U_c/t$  to  $L = \infty$  is difficult from the present data, due to the non-monotonic system-size dependence, as mentioned. However, we can guess that  $U_c/t$  for  $L = \infty$  is only slightly larger than those for finite  $L$ , because the increasing rate of  $U_c/t$  with respect to  $L$  is similar to that for  $t'/t = 0$ .

### 3.2 Confirmation of Mott transition

In this subsection, we confirm that the above transition is a Mott transition by studying various quantities.

First, we consider the doublon-holon binding factor  $\mu$ , which is a good indicator of the Mott transition. In Fig. 4(c), the optimized value of  $\mu$  is plotted as a func-

tion of  $U/t$ . For each  $t'/t$  and  $L$ , except for  $t' = 0$  and  $L = 10$ ,  $\mu$  has a discontinuity and suddenly increases at  $U = U_c$ . Note that for  $U < U_c$ ,  $\mu$  primarily depends on  $t'/t$  and slightly on  $L$  in relation to SC as mentioned later, whereas for  $U > U_c$ ,  $\mu$  sizably increases as  $L$  increases, but is almost independent of  $t'/t$ . Thus, in the strong correlation regime  $U > U_c$ ,  $\mu$  has a value close to 1,<sup>52</sup> which means that a doublon and a holon are almost bound within nearest-neighbor sites. This situation is actually seen in the snapshots taken in the VMC sampling process (Fig. 7). On the weak correlation side of  $U_c$  [Fig. 7(a)], where  $\mu$  has a relatively small value, doublons (negative charge carriers) are often isolated from holons (positive ones). Thus, charge can substantially move, and the system is considered conductive. On the other hand, for  $U > U_c$  [Fig. 7(b)], each doublon is, in most cases, paired with a holon, in addition to the decrease in the carrier number. It follows that free charged particles rarely exist.

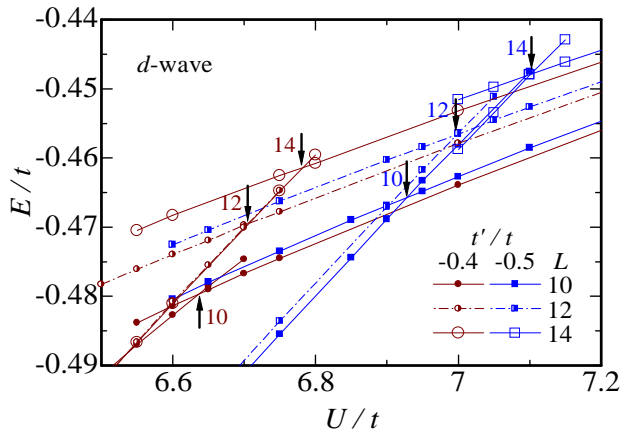


Fig. 6. (Color online) Total energies for strongly frustrated cases ( $t'/t = -0.4$  and  $-0.5$ ) near the critical points indicated by arrows for three system sizes. The behavior of hysteresis is found for every case; the conductive and the insulating cases are denoted by the same symbols. The critical values read  $U_c/t = 6.64, 6.70$  and  $6.78$  for  $L = 10, 12$  and  $14$ , respectively, for  $t'/t = -0.4$ , and similarly  $U_c/t = 6.93, 7.00$  and  $7.10$  for  $t'/t = -0.5$ .

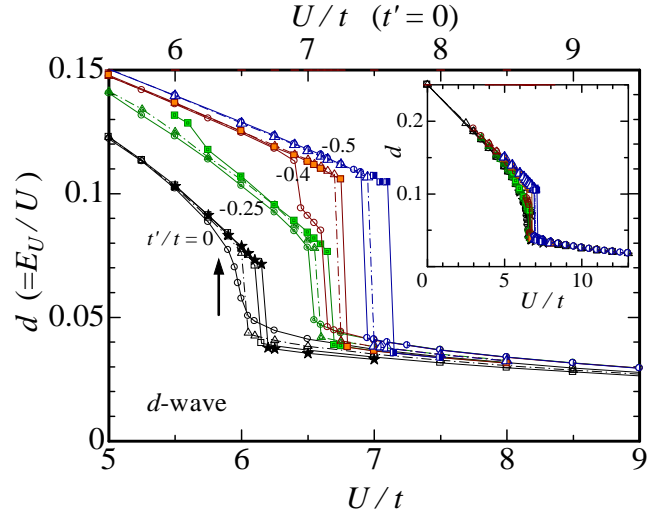
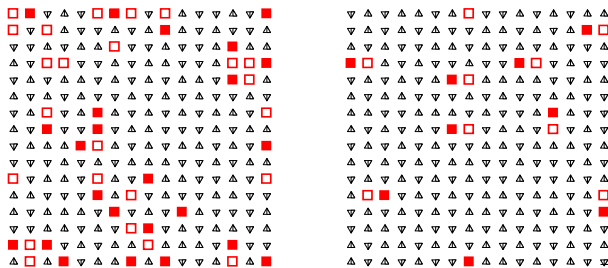


Fig. 8. (Color online) Density of doublon (doubly-occupied sites) obtained with  $\Psi_d$  as a function of  $U/t$  for four values of  $t'/t$ . For each  $t'/t$ , some system sizes ( $L = 10-16$ ) are simultaneously plotted. The symbols are common to Fig. 4. For  $t'/t = 0$ , the horizontal axis is shifted by 0.5 (see upper axis) for clarity. In the inset, the same quantity is shown for a wider range.



(a)  $U < U_c$

(b)  $U > U_c$

Fig. 7. (Color online) Snapshots (typical electron configurations) taken in the VMC sampling process of the  $d$ -wave state for  $t'/t = 0$  and  $L = 16$  ( $U_c/t = 6.69$ ). (a)  $U/t = 6.25$  ( $\mu = 0.30$ ), slightly below  $U_c$ , and (b)  $U/t = 7.50$  ( $\mu = 0.85$ ), slightly over  $U_c$ . Closed and open squares, upward and downward triangles denote doublon, holon,  $\uparrow$ - and  $\downarrow$ -spins, respectively.

Second, we consider the doublon density,

$$d = \frac{1}{N_s} \sum_i n_{i\uparrow} n_{i\downarrow} = \frac{E_U}{U}, \quad (15)$$

which is regarded as the order parameter of Mott transitions,<sup>28,53,54</sup> by analogy with the particle density in gas-liquid transitions. In eq. (15),  $E_U = \langle \mathcal{H}_{\text{int}} \rangle / N_s$ . In the inset of Fig. 8,  $d$  is plotted for four values of  $t'/t$  and for some system sizes. As  $U/t$  increases,  $d$  decreases linearly from the noninteracting value 0.25, but, at  $U = U_c$ , it suddenly drops to a considerably small value, and then decreases slowly for  $U > U_c$ . In the main panel of Fig. 8, the vicinity of the critical point is magnified; the discontinuity of  $d$  at  $U_c$  is clear for each case. This abrupt decrease in doublon number actually can be checked in Fig. 7, where the doublon number is 24 ( $d = 0.094$ ) for

$U/t = 6.25$ , and 9 ( $d = 0.035$ ) for  $U/t = 7.5$ , which is consistent with the values in Fig. 8. Thus, the discontinuity of the doublon density at  $U_c$  is similar to that of the particle density in gas-liquid transitions.

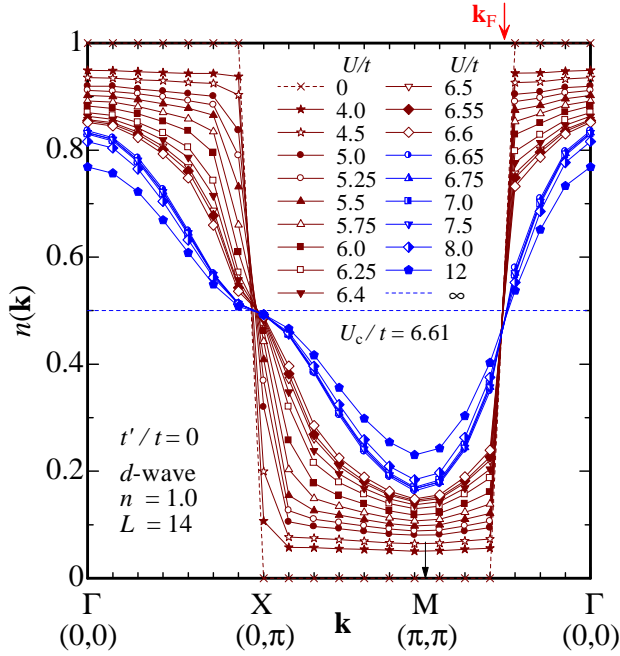


Fig. 9. (Color online) Momentum distribution function of the  $d$ -wave state for various values of  $U/t$  for  $t'/t = 0$ . The brown (blue or half-closed and star) symbols denote the data for  $U < U_c$  ( $U > U_c$ ). The arrow on the upper axis indicates the positions of the Fermi surface in the node-of-gap ( $\Gamma$ -M) direction.

Third, the behavior of the momentum distribution function,

$$n(\mathbf{k}) = \frac{1}{2N_s} \sum_{k,\sigma} \langle c_{\mathbf{k}\sigma}^\dagger c_{\mathbf{k}\sigma} \rangle, \quad (16)$$

at the Fermi surface is another good indicator of the Mott transition. In Fig. 9, we show the  $U/t$  dependence of  $n(\mathbf{k})$  measured with the optimized parameters along the path  $\Gamma(0,0)$ - $X(\pi,0)$ - $M(\pi,\pi)$ - $\Gamma$  in the Brillouin zone for  $t'/t = 0$ . Because the present trial state is a projected  $d$  wave, there is a node in the gap function in the  $\Gamma$ -M direction, and  $n(\mathbf{k})$  should have a discontinuity at the Fermi surface,  $\mathbf{k}_F$ , in this direction if the system is metallic or SC. As shown in Fig. 9, the discontinuity at  $\mathbf{k}_F$  is obvious for  $U < U_c$ , whereas, at  $U = U_c$ , the behavior of  $n(\mathbf{k})$  abruptly changes, and becomes a smooth function for  $U > U_c$  also in the  $\Gamma$ -M direction, that is, the Fermi surface disappears. Thus, metallic properties are abruptly lost at  $U = U_c$  even in the nodal direction of the  $d_{x^2-y^2}$  wave.

To treat this behavior quantitatively, we employ the quasi-particle renormalization factor  $Z$ , which roughly corresponds to the inverse of effective mass, unless the  $\mathbf{k}$ -dependent renormalization of self energy is severe. We have estimated  $Z$  from the magnitude of jump in  $n(\mathbf{k})$  at  $\mathbf{k} = \mathbf{k}_F$  in the nodal direction, and plotted it in Fig. 10 for four values of  $t'/t$ .<sup>55</sup> For all the values of  $t'/t$ ,  $Z$  decreases slowly for  $U < U_c$ , whereas, at  $U = U_c$ ,  $Z$  sud-

denly vanishes with a sizable discontinuity, reflecting the first-order character of the transition. The system-size dependence of  $Z$  is very small, except for minor differences near  $U_c$ . The behavior of  $Z$  strongly suggests that the effective electron mass diverges for  $U > U_c$ .

Finally, let us consider the charge structure factor,

$$N(\mathbf{q}) = \frac{1}{N_s} \sum_{i,j} e^{i\mathbf{q}\cdot(\mathbf{R}_i - \mathbf{R}_j)} \langle n_i n_j \rangle - n^2, \quad (17)$$

with  $n_i = n_{i\uparrow} + n_{i\downarrow}$ . Within the variation theory, it is known that  $N(\mathbf{q}) \propto |\mathbf{q}|$  for  $|\mathbf{q}| \rightarrow 0$ , if the state does not have a gap in the charge degree of freedom, whereas  $N(\mathbf{q}) \propto \mathbf{q}^2$ , if a charge gap opens. In Fig. 11, we show the  $U/t$  dependence of  $N(\mathbf{q})$  for  $t'/t = -0.25$  and  $-0.4$ . For  $U < U_c$ , the behavior of  $N(\mathbf{q})$  near the  $\Gamma$  point seems linear in  $|\mathbf{q}|$  for both values of  $t'/t$ . The behavior of  $N(\mathbf{q})$  abruptly changes at the critical point, and seemingly becomes quadratic in  $|\mathbf{q}|$  for  $U > U_c$ . Although it is not easy to determine definitely the power of  $N(\mathbf{q})$  with the small systems used here, we find that the size dependence is different between for  $U < U_c$  and for  $U > U_c$ . As shown in Fig. 12, the behavior of  $N(\mathbf{q})$  near the  $\Gamma$  point for  $U < U_c$  approaches the analytic curve of  $U/t = 0$  ( $L = \infty$ ) as  $L$  increases. Conversely, for  $U > U_c$ , the slope of  $N(\mathbf{q})$  for  $|\mathbf{q}| \rightarrow 0$  becomes smaller as  $L$  increases, suggesting the quadratic behavior of  $N(\mathbf{q})$ . It follows that  $\Psi_Q^d$  is gapless in the charge sector and conductive for  $U < U_c$ , but a charge gap probably opens for  $U > U_c$  and  $\Psi_Q^d$  becomes insulating.

Due to the behavior of all the quantities discussed above, it is appropriate to judge that a first-order Mott transition takes place in the  $d$ -wave singlet state at  $U = U_c$  for arbitrary values of  $t'/t$  we studied.

### 3.3 Properties of Mott transitions

Most of the properties of the Mott transition in  $\Psi_Q^d$  in the present model eq. (1) are shared with those studied in the preceding report for the anisotropic triangular lattice.<sup>6</sup> In such cases, we avoid repeating detailed explanation, and only give a brief summary.

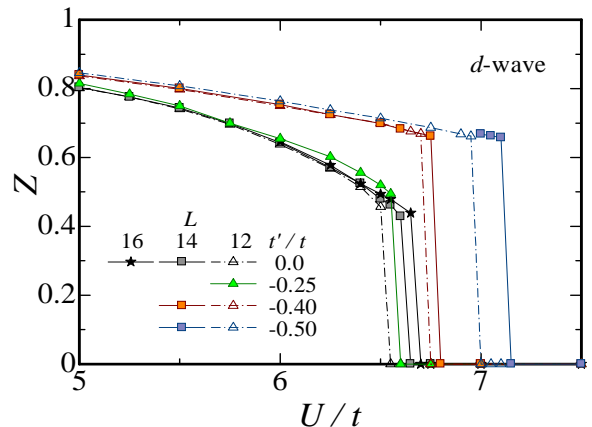


Fig. 10. (Color online) Quasiparticle renormalization factor  $Z$  of the  $d$ -wave singlet states, estimated from the discontinuities of  $n(\mathbf{k})$  in the node-of-gap direction. Data for four values of  $t'/t$  are plotted as a function of  $U/t$ .

(1) In contrast to the behavior in Brinkman-Rice's theory,<sup>53</sup> in which electrons cease moving and doublons completely vanish in the insulating regime, the present VMC result exhibits the energy reduction broadly proportional to  $-t^2/U$  ( $= -J/4$ ) for  $U > U_c$ , as shown in Fig. 13. Thus, as we argued in a previous letter,<sup>8</sup> the results of strong-coupling theories ( $t$ - $J$ -type models) are qualita-

tively useful for  $U > U_c$ , which value is roughly of the bandwidth.<sup>33</sup>

(2) As the frustration  $t'/t$  increases, the character of the first-order phase transition becomes notable. For example, as  $t'/t$  increases, the hysteresis in  $E/t$  is found in smaller systems, and the magnitude of discontinuity at  $U = U_c$  in various quantities increases.

(3) In the insulating regime,  $\Psi_Q^d$  tends to exhibit gap-like behavior in the spin structure factor,

$$S(\mathbf{q}) = \frac{1}{N_s} \sum_{ij} e^{i\mathbf{q}\cdot(\mathbf{R}_i - \mathbf{R}_j)} \langle S_i^z S_j^z \rangle, \quad (18)$$

for small  $|\mathbf{q}|$ . As seen in the inset of Fig. 14 for  $t' = 0$ ,  $S(\mathbf{q})$  is a linear function of  $|\mathbf{q}|$  at  $U/t = 0$ ; as  $U/t$  increases,  $S(\mathbf{q})$  tends to be a quadratic function of  $|\mathbf{q}|$ , suggesting a SC gap opens and becomes large, as will

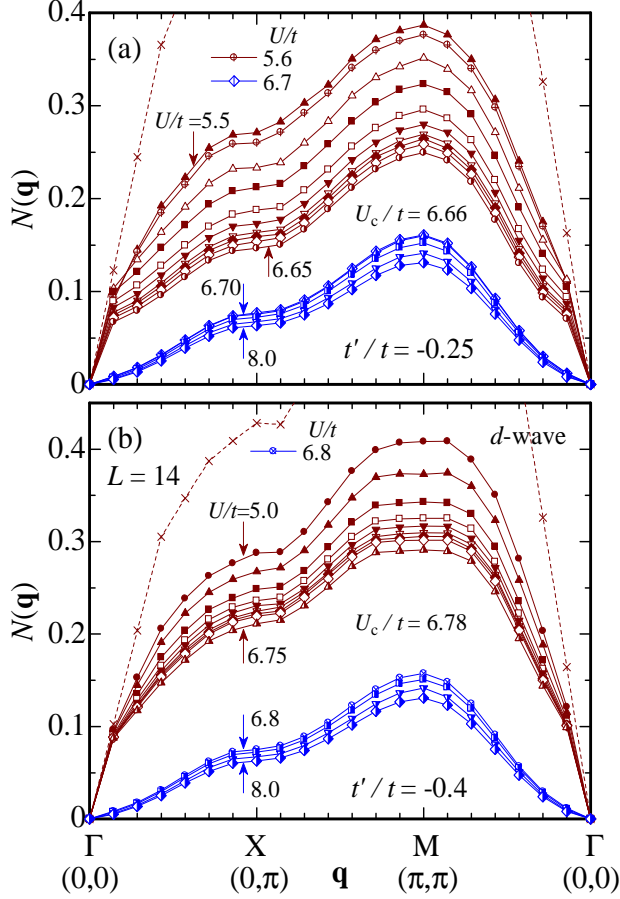


Fig. 11. (Color online)  $U/t$  dependence of the charge structure factor for the  $d$ -wave state ( $L = 14$ ) for (a)  $t'/t = -0.25$  and (b)  $t'/t = -0.4$ . The two panels are in the same scale. The forms of the symbols in both panels are common to Fig. 9 except for the values of  $U/t$  specified here. The brown (blue) symbols denote the data for  $U < U_c$  ( $U > U_c$ ).

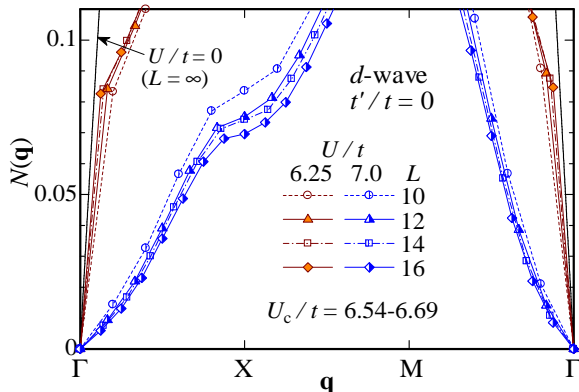


Fig. 12. (Color online) System-size dependence of the charge structure factor in the  $d$ -wave state ( $t'/t = 0$ ) near the  $\Gamma$  point for  $U = 6.25t$  ( $< U_c$ ) and  $U = 7.0t$  ( $> U_c$ ).

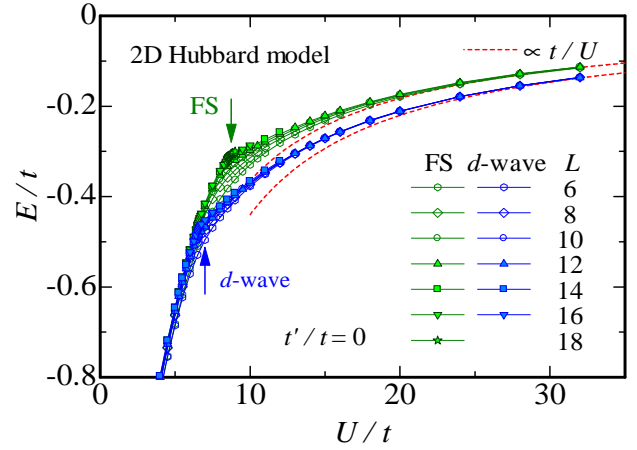


Fig. 13. (Color online) Total energy of the projected Fermi sea and  $d$ -wave states for  $t'/t = 0$  as a function of  $U/t$  for several system sizes. The Mott critical points for both cases are indicated by arrows. Red dashed lines are fitted curves proportional to  $t/U$ . As expected from Fig. 4(f), the results for  $|t'/t| > 0$  almost coincide with the present curves for  $t'/t = 0$  in the insulating regime.

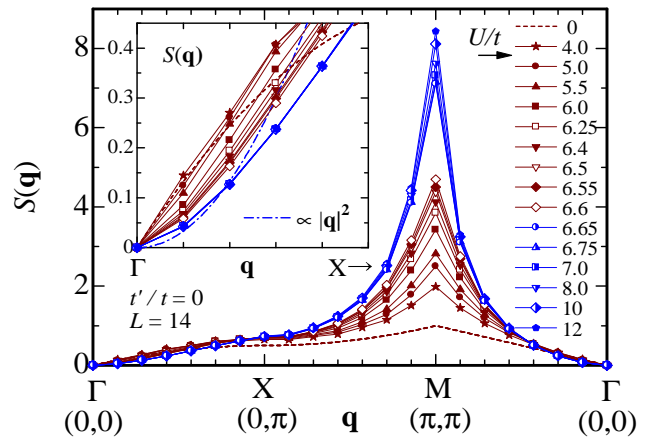


Fig. 14. (Color online)  $U/t$  dependence of the spin structure factor in the  $d$ -wave state for  $t'/t = 0$  and  $L = 14$  ( $U_c/t = 6.61$ ). The brown (blue) symbols denotes data in the conductive (insulating) regime. The inset shows the magnification of the region near the  $\Gamma$  point on the  $\Gamma$ -X line, and the symbols are common to the main panel.  $S(\mathbf{q})$  on the  $\Gamma$ -M line (nodal direction) exhibits basically the same small- $|\mathbf{q}|$  behavior. Data points of different  $U$ 's for  $U > U_c$  almost overlap one another.

Table I. Optimized variational parameters of the two wave functions,  $\Psi_Q^d$  and  $\Psi_Q^{\text{FS}}$ , studied in §4, in the respective insulating regimes ( $U > U_c$ ) for some  $t'/t$ . The last digits include some errors.  $L = 14$ .

$\Psi$	$ t'/t $	$g$	$\Delta_d/t$	$\mu$	$\mu'$	$\zeta/t$
$\Psi_Q^d$ ( $U = 7.5t$ )	0.0	0.266	1.291	0.831	—	0.0
	0.25	0.254	1.339	0.840	-0.0677	0.200
	0.3	0.254	1.335	0.837	-0.0665	0.230
	0.4	0.254	1.349	0.837	-0.0690	0.279
	0.5	0.253	1.355	0.832	-0.0688	0.317
$\Psi_Q^{\text{FS}}$ ( $U = 12t$ )	0.0	0.140	—	0.923	—	—
	0.25	0.119	—	0.904	0.0776	—
	0.4	0.121	—	0.829	0.1317	—

Table II. Three energy components, the total energy and spin structure factor at the AF wave number, calculated with  $\Psi_Q^d$  and  $\Psi_Q^{\text{FS}}$  in the respective insulating regimes ( $U > U_c$ ) for some  $t'/t$ .  $L = 14$ . The last digits include some errors. Because each energy component and  $E/t$  are averaged independently,  $E/t$  does not precisely coincide with the sum of the components.

$\Psi$	$ t'/t $	$E_t/t$	$E_{t'}/t$	$E_U/t$	$E/t$	$S(\mathbf{G})$
$\Psi_Q^d$ ( $U = 7.5t$ )	0.0	-0.6922	0.0	0.2548	-0.4384	7.54
	0.25	-0.6888	-0.0008	0.2533	-0.4375	7.28
	0.3	-0.6899	-0.0012	0.2532	-0.4370	7.27
	0.4	-0.6848	-0.0019	0.2529	-0.4357	7.06
	0.5	-0.6829	-0.0033	0.2522	-0.4340	6.90
$\Psi_Q^{\text{FS}}$ ( $U = 12t$ )	0.0	-0.4383	0.0	0.1809	-0.2575	15.93
	0.25	-0.3455	-0.0018	0.1576	-0.1899	3.81
	0.4	-0.3276	-0.0053	0.1573	-0.1752	2.09

be mentioned in §5. For  $U > U_c$ , the quadratic behavior of  $S(\mathbf{q})$  becomes more obvious; it is possible that a spin gap opens in the insulating regime. As discussed later, the frustration makes no difference in this point. This gap-like behavior is in contrast to the case of  $\Psi_Q^{\text{FS}}$ , as will be argued in §4. Strictly, however, the insulating state represented by  $\Psi_Q^d$  can be gapless in the spin sector, in the same sense as the  $d$ -wave SC is gapless in the node direction. To settle this point, further studies are necessary.

(4) In the preceding study for the anisotropic triangular lattice,<sup>6</sup> a band renormalization effect<sup>46</sup> is taken into account by optimizing  $t'$  in  $\Psi_Q^d$  as a variational parameter, independently of  $t'$  given in the Hamiltonian. In the insulating regime, the effective  $t'$  is greatly reduced to an almost nonfrustrated value, namely  $t'/t \sim 0$ . Thereby, the Fermi surface almost recovers the nesting condition for the square lattice, leading to highly developed short-range AF correlation. In the trial states studied here, the band renormalization effect is not included, but the various results are quantitatively similar to those of the previous work, and the AF correlation considerably develops for  $U > U_c$ , as seen in Figs. 14 and 25. This result is mainly caused by the behavior of the chemical potential  $\zeta$  [Fig. 4(e)],<sup>56</sup> which changes its sign for  $U > U_c$  so as to recover the nesting condition, instead of the band renormalization.

(5) In Table I, we show the optimized parameter values in the insulating regime ( $U > U_c$ ) for some  $t'/t$ . Note

that the parameters vary only very slightly, except for  $\zeta$ ; the optimized  $\Psi_Q^d$  is almost unchanged with varying  $t'/t$ . In Table II, we list the total energy and energy components for  $U > U_c$ , calculated with the optimized  $\Psi_Q^d$ .  $E$  is again almost independent of  $t'/t$ , because  $E_{t'}$  makes a very slight contribution even for large  $t'/t$  (see also Table III). As shown in the last column of Table II, the AF spin correlation preserves a considerably large value up to large  $t'/t$ . This indicates that  $\Psi_Q^d$  is stabilized by preserving the nesting condition for the square lattice, in other words, retaining the quasi Fermi surface at the gap maxima  $(\pi, 0)$  and  $(0, \pi)$ , at the cost of the energy reduction due to the diagonal hopping or frustration. Thus, the AF correlation is a key factor to stabilize  $\Psi_Q^d$ .

Regarding the AF correlation, it is known for the SC states with  $d$ -type symmetries that the gap maxima overlap with the hot spot, namely the intersection of the Fermi surface and the magnetic Brillouin zone boundary.<sup>44</sup> Thus, it is possible that the shape of the gap function  $\Delta_{\mathbf{k}}$  deviates from the simple  $d$  wave, especially for large  $t'/t$ . It is an interesting future problem.

#### 4. Mott Transitions in Projected Fermi Sea

In this section, we pursue the Mott transition in  $\Psi_Q^{\text{FS}}$ , as a continuation of the previous studies for  $t'/t = 0$ .<sup>8,38</sup> This transition has features different from those of  $\Psi_Q^d$ , although  $\Psi_Q^{\text{FS}}$  always has a higher energy than  $\Psi_Q^d$  within the present model eq. (1). In §4.1, we make a careful analysis for  $t' = 0$ . In §4.2, we consider the  $t'/t$  dependence, and contrast the properties with those in  $\Psi_Q^d$ .

##### 4.1 Case for $t' = 0$

The existence of a Mott transition in  $\Psi_Q^{\text{FS}}$  for  $t'/t = 0$  was first pointed out in ref. 38, in which the critical value is estimated as  $U_c/t \sim 8.8$  by checking the cusp-like behavior in energy components and the discontinuity in  $n(\mathbf{k})$  for  $L = 10$  and 12. In these sizes, the transition looked like a continuous type. Certainly, we can find cusp-like behavior in Fig. 13 [or in the main panel of Fig. 15(d)], where the  $U/t$  dependence of total energy is shown. Because the system-size dependence is considerably large near the cusp, we show the magnification in the vicinity of the cusp in the inset of Fig. 15(d). For  $L \leq 14$ ,  $E/t$  is a smooth function of  $U/t$  and has a unique optimized value, whereas, for  $L = 16$  and 18,  $E/t$  exhibits hysteresis or double-minimum behavior around  $U = U_c = 8.59t$  and  $8.73t$ , respectively, like the case of  $\Psi_Q^d$  studied in the preceding section. Correspondingly, the two variational parameters,  $g$  and  $\mu$ , exhibit discontinuities at  $U_c$  for  $L \geq 16$ , as shown in Figs. 15(a) and (b), although their magnitude is small compared with that of  $\Psi_Q^d$  in Figs. 4(a) and (c). Thus, this transition, at least for  $t'/t = 0$ , is ascertained as of first order.

In Fig. 16, the doublon density is plotted as a function of  $U/t$ . At the critical point  $U_c$ , the order parameter of Mott transitions  $d$  has a discontinuity for  $L \geq 16$ , and suddenly drops to small values. Simultaneously, the doublon-holon binding parameter  $\mu$  becomes large and approaches 1, as shown in Fig. 15(b). These results again suggest that this transition is a Mott transition with the

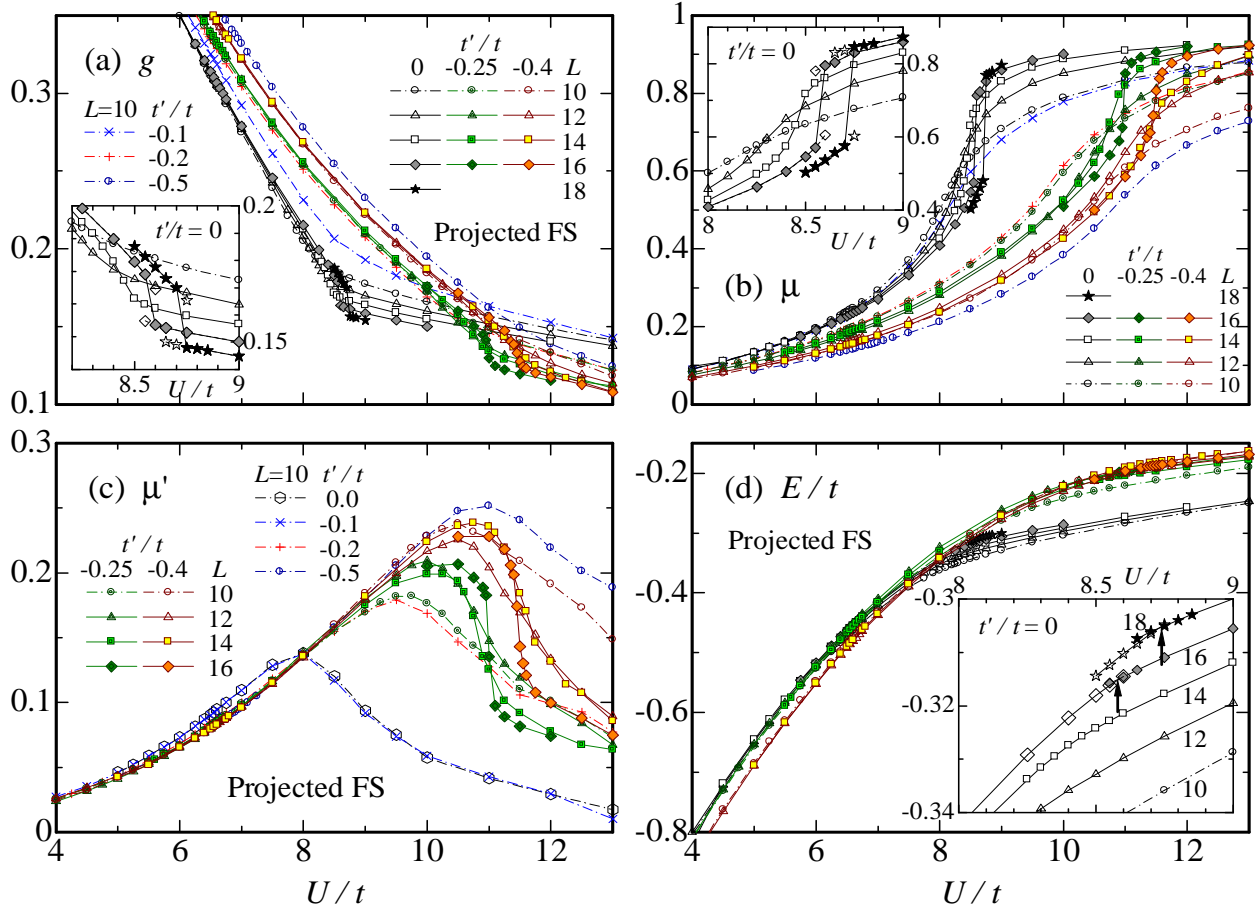


Fig. 15. (Color online) (a)-(c) Optimized variational parameters (at the global minima of  $E/t$ ) for the projected Fermi sea  $\Psi_Q^{\text{FS}}$  as a function of  $U/t$ : (a) Onsite correlation (Gutzwiller) factor. (b) Doubly-holon binding factor between the nearest-neighbor sites. The insets in (a) and (b) are magnifications near  $U_c$  for  $t'/t = 0$ . The data of local (but not global) minima for  $L = 16$  and  $18$  are added using open symbols. (c) The same factor between the diagonal-neighbor sites. (d) Optimized total energies for  $t'/t = 0, -0.25$  and  $-0.4$ . Data for several system sizes are compared. The inset represents a magnification near  $U_c$  for  $t'/t = 0$ . For the data of  $L = 16$  and  $18$ , open (closed) symbols are used for the metallic (insulating) regime to emphasize the hysteresis behavior. The critical values indicated by arrows are  $U_c/t = 8.59$  and  $8.73$  for  $L = 16$  and  $18$ , respectively. The symbols without special mention and the scales in abscissa are common to all the main panels. In (c), we add the data of  $\Psi_Q^{\text{FS}}$  including  $\mu'$  for  $t'/t = 0$ . Although  $\mu'$  has a finite value in the metallic region, its effect is almost negligible.

doublon-holon binding mechanism similar to that of  $\Psi_Q^d$ . Actually, we have verified that the feature of electron configurations is quite different between for  $U < U_c$  and for  $U > U_c$  (not shown), just like in Fig. 7.

The transition is corroborated by the behavior of  $n(\mathbf{k})$  and  $N(\mathbf{q})$ , in the same way as the  $d$ -wave state. In Fig. 17,  $n(\mathbf{k})$  [eq. (16)] is plotted along the path  $\Gamma$ -X-M- $\Gamma$  for various values of  $U/t$ . Because  $\Psi_Q^{\text{FS}}$  is metallic for  $U < U_c$ , the Fermi surface is defined in any direction; in this path,  $\mathbf{k}_F$  is located at the X point and the midpoint of the  $\Gamma$ -M segment. For  $U < U_c$ , the discontinuities are apparent at both points of  $\mathbf{k}_F$ , whereas for  $U > U_c$ , discontinuities vanish, indicating a gap opening. In Fig. 18, we show the magnitude of discontinuity,  $Z$ , measured at the X point, because the extrapolation error is small. As  $U/t$  increases, the quasiparticle renormalization factor,  $Z$ , monotonically decreases, and vanishes at  $U_c$ ; the effective mass diverges and  $\Psi_Q^{\text{FS}}$  becomes insulating. For  $L \leq 14$ ,  $Z$  is continuous near  $U_c$ , as reported in Fig. 17 in ref. 38, whereas  $Z$  has an appreciable discontinuity at  $U_c$  for  $L \geq 16$  and probably for  $L = \infty$ . Incidentally, the discontinuity in  $Z$  in  $\Psi_Q^{\text{FS}}$  is smaller than that in  $\Psi_Q^d$

(Fig. 10); the character of the first-order transition is less conspicuous in  $\Psi_Q^{\text{FS}}$ . In contrast, in a dynamical mean-field theory for the hypercubic lattice,<sup>57</sup>  $Z$  continuously decreases and vanishes at  $U = U_c$  without a jump.

In Fig. 19,  $N(\mathbf{q})$  [eq. (17)] is plotted for various values of  $U/t$ . The behavior for small  $|\mathbf{q}|$  is basically the same as that for  $\Psi_Q^d$  [Fig. 11], namely,  $N(\mathbf{q}) \propto |\mathbf{q}|$  for  $U < U_c$  (brown symbols), whereas  $N(\mathbf{q})$  tends to be proportional to  $\mathbf{q}^2$  for  $U > U_c$  (blue symbols). It follows a charge gap opens for  $U > U_c$ .

From all the above results, we regard this transition as an Mott (metal-to-nonmagnetic-insulator) transition, which is caused by the doublon-holon binding mechanism, basically in the same way as in  $\Psi_Q^d$ .

Finally, we look into the spin degree of freedom. In Fig. 20,  $S(\mathbf{q})$  [eq.(18)] is plotted for various values of  $U/t$ . As  $U/t$  increases, the AF correlation  $S(\mathbf{G})$  increases, especially abruptly near the critical point. Although the behavior of  $S(\mathbf{q})$  is as a whole similar to the case of  $\Psi_Q^d$  (Fig. 14),  $S(\mathbf{G})$  is twice larger for  $\Psi_Q^{\text{FS}}$ . However, the

sublattice magnetization,

$$m = \frac{1}{N_s} \left| \sum_i e^{i\mathbf{G}\cdot\mathbf{r}_i} \langle S_i^z \rangle \right|, \quad (19)$$

remains zero within the statistical fluctuation. Thus, a long-range order is not realized, although the AF correlation is considerably enhanced in the insulating regime. Note that the behavior of  $S(\mathbf{q})$  for  $|\mathbf{q}| \rightarrow 0$  is linear in  $|\mathbf{q}|$  for arbitrary  $U/t$ , as shown in the insets of Fig. 20, in contrast to the case of  $\Psi_Q^d$  (inset of Fig. 14). This strongly suggests that the spin gap is absent. Thus,  $\Psi_Q^{\text{FS}}$  for  $U > U_c$  represents a nonmagnetic insulator without a spin gap, which is considered to be realized in  $\kappa\text{-(ET)}_2\text{Cu}_2(\text{CN})_3$ .<sup>58</sup>

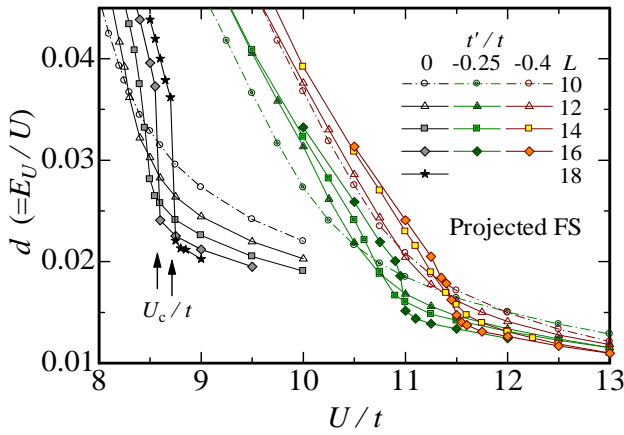


Fig. 16. (Color online) The behavior of doublon density  $d$  near the Mott critical points in the projected Fermi sea  $\Psi_Q^{\text{FS}}$  for three values of  $t'/t = 0$ . Data of several system sizes are plotted for each  $t'/t$ . For  $t'/t = 0$  and  $L = 16$  and  $18$ , the critical values of first order transitions are indicated by arrows.

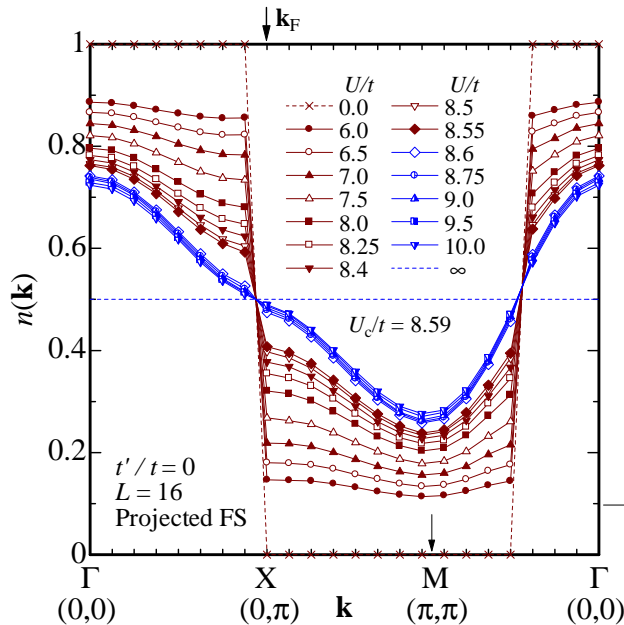


Fig. 17. (Color online)  $U/t$  dependence of the momentum distribution function of  $\Psi_Q^{\text{FS}}$  for  $t'/t = 0$ . Data points in the metallic (insulating) regime are denoted by brown (blue) symbols and lines. In this case,  $Z$  (Fig. 18) is measured at  $\mathbf{k}_F$  indicated by an arrow on the upper axis (X point).

#### 4.2 Effect of frustration

First, we consider the effect on the properties of the transition. In Figs. 15(a)-(c), we show the optimized variational parameters for  $t'/t = -0.25$  and  $-0.4$ , besides  $t' = 0$ , for systems up to  $L = 16$ . Let us consider the doublon-holon binding parameter  $\mu$  [Fig. 15(b)] as a typical one. For small systems (e.g.  $L = 10$ ),  $\mu$  is a more smooth ‘S’-shaped function of  $U/t$  than that for  $t' = 0$ . As the system size increases,  $\mu$  abruptly represents semi-critical behavior at somewhat larger  $U/t$  than that for  $t' = 0$  [ $U_c/t \sim 10.95$  (11.45) for  $t'/t = -0.25$  ( $-0.4$ ) for  $L = 16$ ]. In contrast to the case of  $t' = 0$ , the cases of  $t'/t = -0.25$  and  $-0.4$  do not give an indication of a first-order transition like discontinuity or hysteresis even for  $L = 16$ . In comparing the results among the three values of  $t'/t$ , we notice that the critical behavior tends to be more continuous, as the frustration becomes strong. We do not treat larger systems in this work, because the statistical fluctuation around the critical points becomes rapidly larger as  $L$  increases. However, we guess that this size-dependent critical behavior is a sign of a first-order

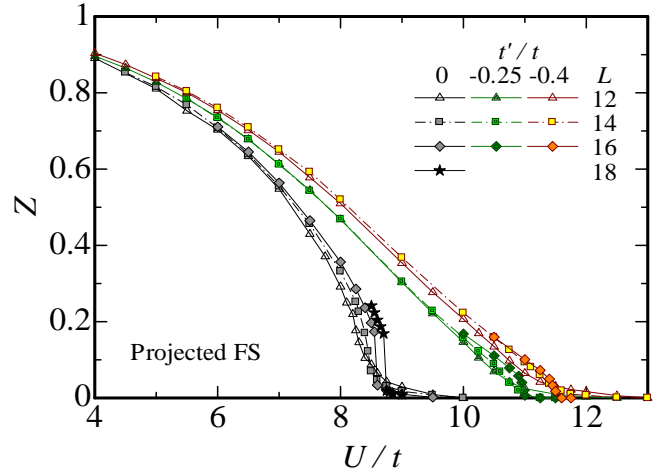


Fig. 18. (Color online) Quasiparticle renormalization factor  $Z$  of the projected Fermi sea, estimated from the discontinuities of  $n(\mathbf{k})$  on the X-M line in the Brillouin zone. Data for three values of  $t'/t$  and some system sizes are plotted as a function of  $U/t$ . The tails for  $U > U_c$  are mainly caused by finite-sized effects.

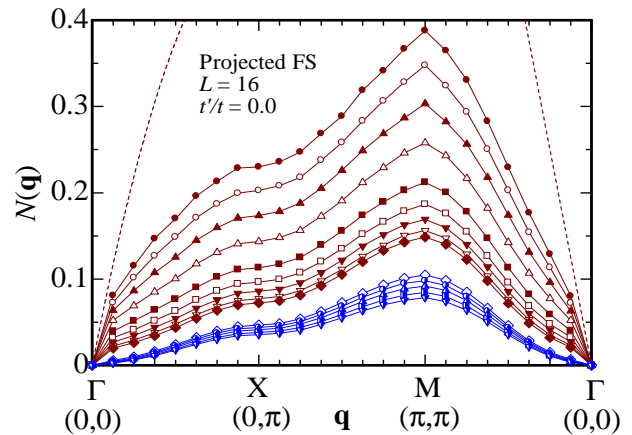


Fig. 19. (Color online)  $U/t$  dependence of the charge density structure factor of  $\Psi_Q^{\text{FS}}$  for  $t'/t = 0$ . The symbols denote the same values of  $U/t$  as in Fig. 20.  $U_c/t = 8.59$ .

Table III. Comparison of the ratio  $\rho = E_{t'}/E_t$  among the different phases indicated in the bracket for the  $d$ -wave state and the projected Fermi sea. The abbreviations ‘ins.’ and ‘wSC’ denote insulating and weak SC, respectively. The systems of  $L = 14$  is used. Data of  $\rho$  are shown in the percentage.

$\Psi$	$ t'/t $	$U/t$			
		0	6.25	7.5	13
$\Psi_Q^d$	0.25	3.3	1.4 (SC)	0.12 (ins.)	—
	0.4	8.8	7.6 (wSC)	0.28 (ins.)	—
$\Psi_Q^{\text{FS}}$	0.25	3.3	3.3 (metal)	3.2 (metal)	0.4 (ins.)
	0.4	8.8	8.8 (metal)	8.5 (metal)	1.1 (ins.)

transition.

These features can be seen in the other variational parameters [Figs. 15(a) and (c)], total energy [Fig. 15(d)] doublon density (Fig. 16), quasi-particle renormalization factor (Fig. 18), and so on. The feature that the critical properties tends to be continuous as  $t'/t$  increases is opposite to that of  $\Psi_Q^d$  studied in §3, but similar to that of the path-integral-renormalization-group approach.<sup>17</sup>

Next, we consider the effect of frustration on the insulating state. As shown in Table I, when  $t'/t$  varies, the optimized parameters, namely the wave function, appreciably changes, in contrast to that of  $\Psi_Q^d$ . Accordingly, the physical quantities with respect to  $\Psi_Q^{\text{FS}}$  varies with the variation of  $t'/t$ , as seen in Table II. As for energy, a notable point is that the contribution of  $E_{t'}$  is still strongly suppressed in  $\Psi_Q^{\text{FS}}$ , similarly to that for  $\Psi_Q^d$ . To see definitely how  $E_{t'}$  behaves when  $U/t$  varies, we list the ratio  $\rho \equiv E_{t'}/E_t$  in the different phases in Table III.  $\rho$  almost preserves the value of the noninteracting case ( $U = 0$ ) in the metallic phase, but, in the insulating phase,  $\rho$  drops to a very small value, although not so small as in  $\Psi_Q^d$ . This feature is influenced by  $\mu'$ . As seen in Fig. 15(c),  $\mu'$  abruptly diminishes at  $U_c$ , meaning the doublon-holon binding in the diagonal direction, which assists local diagonal hopping for large  $U/t$ , becomes less advantageous for  $U > U_c$  also in  $\Psi_Q^{\text{FS}}$ . The decrease in  $\mu'$

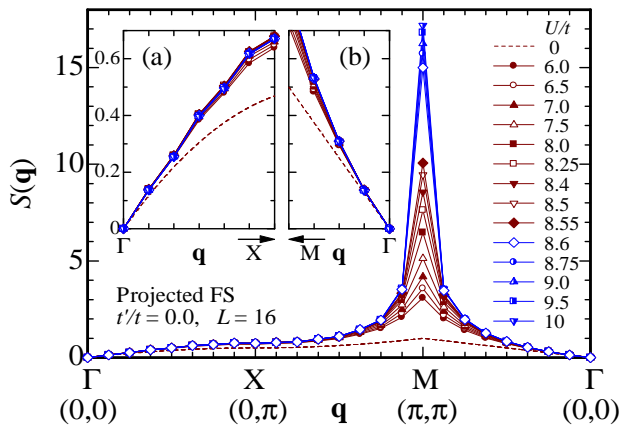


Fig. 20. (Color online)  $U/t$  dependence of the spin structure factor of the projected Fermi sea for  $t'/t = 0$ . The brown (blue) symbols denote the metallic (insulating) regime.  $U_c/t = 8.59$ . The insets are the close-ups near the  $\Gamma$  point on (a) the  $\Gamma$ - $M$  line, and (b) the  $\Gamma$ - $X$  line.

is anticipated for the enhancement of the AF correlation, mentioned next.

Returning to Table II, we find that the AF spin correlation  $S(\mathbf{G})$  markedly develops for  $t'/t = 0$ , but drastically diminishes as  $|t'/t|$  increases, in sharp contrast with that of  $\Psi_Q^d$ . To elucidate the situation, we plot  $S(\mathbf{q})$  for  $t'/t = -0.25$  and  $-0.4$  in Figs. 21(a) and (b), respectively (cf. also Fig. 20 for  $t' = 0$ ). Although the magnitude of  $S(\mathbf{G})$  abruptly decreases as  $|t'/t|$  increases from 0 to 0.25, the peak position of  $S(\mathbf{q})$  remains at  $\mathbf{q} = \mathbf{G}$ . For  $t'/t = -0.4$ , however, in addition to the successive decrease in magnitude, the peak of  $S(\mathbf{q})$  moves to incommensurate wave numbers near the M point.

Thus, the effect of frustration is explicitly reflected in physical quantities estimated with the insulating state of  $\Psi_Q^{\text{FS}}$ .

## 5. $d_{x^2-y^2}$ -wave Superconductivity

In this section, we study the properties of SC arising in the  $d$ -wave singlet state  $\Psi_Q^d$ . In §5.1, we deduce the area where SC appears in the  $t'$ - $U$  plane by distinguishing, in the condensation energy, between the contributions from a SC gap and from an insulating gap. In §5.2, we confirm the appearance of SC by directly observing the  $d$ -wave pairing correlation function. In §5.3, we consider the origin of this SC.

### 5.1 Condensation energy

First, to know the stability of the  $d$ -wave singlet state  $\Psi_Q^d$ , we consider its condensation energy given by

$$\Delta E = E(\Psi_Q^d) - E(\Psi_Q^{\text{F}}), \quad (20)$$

where  $E(\Psi)$  denotes the optimized variational energy per site with respect to  $\Psi$ . In Fig. 22(a),  $\Delta E/t$  for various  $t'/t$  is plotted as a function of  $U/t$ ; in Fig. 22(b), the region near the Mott critical points ( $U_c/t$ ) is magnified.

Because the behavior of  $\Delta E$  is different according to the value of  $t'/t$ , we first consider the weakly frustrated cases ( $t'/t \lesssim 0.3$ ). As pointed out in ref. 8, for small values of  $U/t$  ( $\lesssim 5$ ),  $\Delta E/t$  is extremely small; at an intermediate value of  $U$  ( $= U_{\text{onset}} \sim 5t-6t$ ),  $\Delta E/t$  starts to

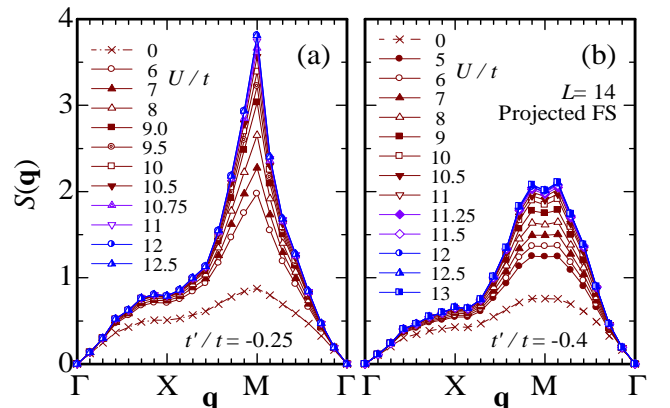


Fig. 21. (Color online)  $U/t$  dependence of the spin structure factor of the projected Fermi sea for (a)  $t'/t = -0.25$  and (b)  $-0.4$ . The brown (violet, blue) symbols denote the metallic (transient, insulating) regime. The scale in the vertical axis is common to both panels.

increase slowly at first, then abruptly at the Mott critical value  $U_c$  of  $\Psi_Q^d$ , where, in some cases, we can observe a mild cusp in Fig. 22(b). As  $U/t$  increases further,  $\Delta E/t$  has a maximum and then slowly decreases. We are now aware (§3) that, for  $U > U_c$ ,  $\Psi_Q^d$  becomes an insulating state. Hence, the marked increase of  $\Delta E$  in this regime is considered to originate in the insulating  $d$ -wave gap.<sup>45</sup> Consequently, the region where substantial energy reduction due to a SC gap is restricted to  $U_{\text{onset}} \lesssim U < U_c$ . This idea is supported by the behavior  $d$ -wave gap parameter  $\Delta/t$ , which exhibits an appreciable increase for the corresponding values of  $U/t$  and  $t'/t$ , as shown in Fig. 4(b). Incidentally, the doublon-holon binding parameter  $\mu$  increases very similarly to  $\Delta/t$  [Fig. 4(c)], suggesting that this binding plays an active role for the  $d$ -wave pairing in the nearest-neighbor sites.

Next, we proceed to the strongly frustrated cases ( $t'/t \gtrsim 0.4$ ). A major feature of  $\Delta E$  different from the weakly frustrated case is no substantial increase for  $U_{\text{onset}} \lesssim U < U_c$ . As seen in Fig. 22(b), we cannot determine  $U_{\text{onset}}$  for  $t'/t = -0.4$  and  $-0.5$ , except for a special case,  $t'/t = -0.4$  and  $L = 10$ .<sup>59</sup> Correspondingly, the increase in the  $d$ -wave gap  $\Delta/t$  [Fig. 4(b)] is firmly suppressed in the conductive region ( $U < U_c$ ), compared with the weakly frustrated cases. The behavior of  $\mu$  [Fig. 4(c)] again follows that of  $\Delta/t$ . Thus, SC is expected to be weak, if any, in this regime.

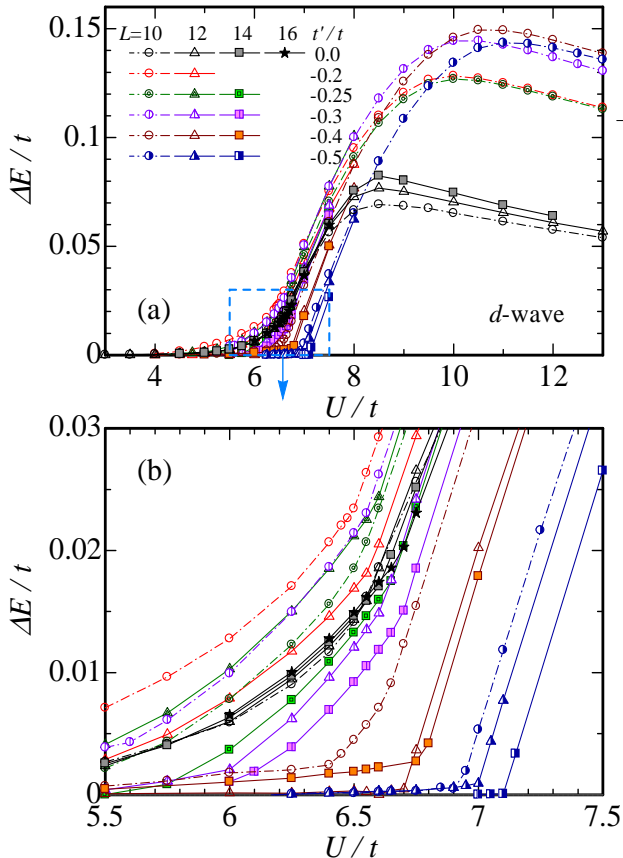


Fig. 22. (Color online) Condensation energy,  $\Delta E/t$ , of the  $d$ -wave singlet state as a function of  $U/t$  for various values of  $t'/t$  and  $L$ . (a)  $\Delta E/t$  in a wide range of  $U/t$ . (b) A close-up of  $\Delta E/t$  near the Mott critical points; the range is indicated by a sky-blue dashed line in (a). The symbols are common to (a) and (b).

Incidentally, we notice that the value of  $U/t$  at the maximum of  $\Delta E/t$  in the insulating regimes approximately corresponds to the Mott critical point of  $\Psi_Q^{\text{FS}}$ ,  $U_c^{\text{FS}}/t$ , considered in §4.  $U_c^{\text{FS}}/t$  also corresponds to the crossover value where the character of SC changes from the interaction-energy origin to the kinetic-energy origin.<sup>8</sup>

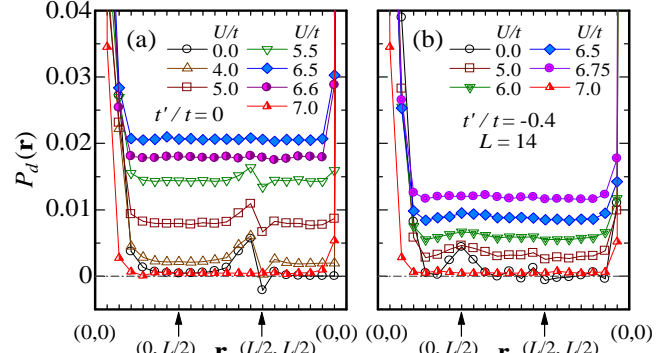


Fig. 23. (Color online) Real-space pair correlation function of the  $d$ -wave symmetry along the path of  $\mathbf{r}$ ,  $(0,0)$ - $(0,L/2)$ - $(L/2,L/2)$ - $(0,0)$ , for various values of  $U/t$ . (a)  $t'/t = 0$  and (b)  $t'/t = -0.4$ , both for  $L = 14$ . The scale of the ordinate axis is common to both panels. The data are obtained, using VMC calculations for  $U \neq 0$ , and from the analytic formula for  $U = 0$ .

## 5.2 Pair correlation function

To confirm directly the appearance of  $d_{x^2-y^2}$ -wave SC, the  $d$ -wave nearest-neighbor pair correlation function  $P_d(\mathbf{r})$  is convenient for the present approach:<sup>60</sup>

$$P_d(\mathbf{r}) = \frac{1}{N_s} \sum_i \sum_{\tau, \tau' = \hat{x}, \hat{y}} (-1)^{1-\delta(\tau, \tau')} \times \langle \Delta_{\tau}^{\dagger}(\mathbf{R}_i) \Delta_{\tau'}(\mathbf{R}_i + \mathbf{r}) \rangle, \quad (21)$$

in which  $\hat{x}$  and  $\hat{y}$  denote the lattice vectors in the  $x$  and  $y$  directions, respectively, and  $\Delta_{\tau}^{\dagger}(\mathbf{R}_i)$  is the creation operator of a nearest-neighbor singlet,

$$\Delta_{\tau}^{\dagger}(\mathbf{R}_i) = (c_{i\uparrow}^{\dagger} c_{i+\tau\downarrow}^{\dagger} + c_{i+\tau\uparrow}^{\dagger} c_{i\downarrow}^{\dagger}) / \sqrt{2}. \quad (22)$$

If  $P_d(\mathbf{r})$  has a finite value for  $|\mathbf{r}| \rightarrow \infty$ , an off-diagonal long-range order exists. For finite systems, however, we have to appropriately determine long-distance values of  $P_d(\mathbf{r})$ , especially, in the cases of small  $U/t$  where the correlation length is long. In Fig. 23,  $P_d(\mathbf{r})$  is plotted for two values of  $t'/t$ . Although  $P_d(\mathbf{r})$  for large  $|\mathbf{r}|$  should vanish for  $U/t = 0$ , spikes of sizable magnitude appears near  $\mathbf{r} = (L/2, L/2)$  [ $(0, L/2)$ ] for  $t'/t = 0$  [ $-0.4$ ] in this system size.<sup>61</sup> Furthermore, the trace of this spike structure remains for fairly large values of  $U/t$ . Thus, for small  $U/t$ , we should consider  $P_d(\mathbf{r})$  which does not have peculiar finite-sized effects. Fortunately, we found that, in the noninteracting cases, the magnitude of  $|P_d(\mathbf{r})|$  for  $\mathbf{r} = (L/2 - 1, L/2)$ , which is an almost farthestmost point, is very small (less than  $10^{-4}$ ) for arbitrary values of  $t'/t$  and  $L$ . Hence, we employ it as the large- $|\mathbf{r}|$  value,  $P_d^{\infty}$ , for small  $U/t$ , namely  $0 \leq U \leq U_{\text{max}}$  with  $U_{\text{max}}$  being the

value at which  $P_d(\mathbf{r})$  becomes maximum. For the strong-correlation regimes ( $U > U_{\max}$ ),  $P_d(\mathbf{r})$  becomes almost constant for  $|\mathbf{r}| \geq 3$ ,<sup>62,63</sup> as shown in Fig. 23. Hence, in these regimes, we average  $P_d(\mathbf{r})$ 's with  $|\mathbf{r}| \geq 3$  for  $P_d^\infty$ .

In Figs. 24(a) and (b),  $P_d^\infty$  thus obtained is plotted as a function of  $U/t$ . In the weakly correlated regime ( $U/t \lesssim 4$ ), the increase in  $P_d^\infty$  is small, irrespective of the value of  $t'/t$ . For weakly frustrated cases ( $|t'/t| \lesssim 0.3$ ),  $P_d^\infty$  starts to increase appreciably at  $U \sim U_{\text{onset}}$  as  $U/t$  increases, has a peak at  $U/t = 6-6.25$ , and then abruptly decreases at the Mott critical point  $U = U_c$ . The system-size dependence of  $P_d^\infty$  near the peak is weak for  $L \geq 12$ . Thus, in this cases, robust  $d$ -wave SC certainly takes place for  $U_{\text{onset}} \lesssim U < U_c$ . On the other hand, for strongly frustrated cases [ $|t'/t| \gtrsim 0.4$  in Fig. 24(b)], no sizable increase of  $P_d^\infty$  is found at the value corresponding to  $U_{\text{onset}}$ .  $P_d^\infty$  slowly and monotonically increases until it abruptly drops at  $U = U_c$ .<sup>59</sup> Moreover, the system-size dependence is very large. Eventually, robust  $d$ -wave SC occurs in the limited area,  $U_{\text{onset}} \lesssim U < U_c$  and  $|t'/t| \lesssim 0.3$ , within  $\Psi_Q^d$ . A similar result has been recently obtained by a fluctuation exchange approximation.<sup>64</sup>

In Fig. 24(c), we show the magnification of  $P_d^\infty$  near the Mott critical point. In the insulating regime ( $U > U_c$ ),  $P_d^\infty$  becomes almost independent of  $t'/t$ , as mentioned in the item (5) in §3.3, decreases rapidly as the system size  $L$  increases, and probably vanishes in the limit of  $L \rightarrow \infty$ . Because the statistical fluctuation in the VMC data is much smaller in the insulating regime than in the conductive regime, the data are more reliable. The disappearance of  $P_d^\infty$  for  $U > U_c$  is quite justifiable as an insulating state.

### 5.3 Properties of superconductivity

First, we study the relation between  $d$ -wave SC and AF correlation. In Figs. 14 and 25(a) and (b),  $U/t$  dependence of  $S(\mathbf{q})$  in  $\Psi_Q^d$  is depicted for  $t'/t = 0, -0.3$  and  $-0.4$ , respectively. As mentioned, robust SC arises for  $t'/t = 0$  and  $-0.3$ , but does not for  $t'/t = -0.4$  [Fig. 24]. This is supported by the small- $|\mathbf{q}|$  behavior of  $S(\mathbf{q})$ , shown in the insets of Fig. 25. For  $t'/t = -0.3$ ,  $S(\mathbf{q})$  for small  $|\mathbf{q}|$  tends to be quadratic in  $|\mathbf{q}|$  as  $U/t$  increases, indicating a SC gap develops, whereas for  $t'/t = -0.4$ ,  $S(\mathbf{q})$  remains almost linear in  $|\mathbf{q}|$ .

We now focus on the AF wave number  $\mathbf{G}$ . For  $U = 0$ ,  $S(\mathbf{q})$  has a pointed peak for  $t' = 0$ , a rounded peak for  $t'/t = -0.3$  and a flat top for  $-0.4$ , due to the frustration. For the cases of  $t'/t = 0$  and  $-0.3$ , in which robust SC appears,  $S(\mathbf{G})$  steadily grows as  $U/t$  increases even in the conductive regime,  $U < U_c$  [Figs. 14 and 25(a)]. In the strongly frustrated case ( $t'/t = -0.4$ ), in which the SC correlation does not develop, the magnitude of  $S(\mathbf{G})$  reaches no more than a half of that for  $t'/t = -0.3$ , although  $S(\mathbf{q})$  somewhat increases for  $U < U_c$  [Fig. 25(b)]. To see the  $t'/t$  dependence of  $S(\mathbf{q})$  explicitly, we plot  $S(\mathbf{q})$  for various values of  $t'/t$  in Fig. 26(a) at  $U/t = 6$ , near which  $P_d^\infty$  has a maximum (see Fig. 24). When  $t'/t$  is varied, the change in  $S(\mathbf{q})$  is quantitatively insignificant except near the M point. As  $|t'/t|$  increases,  $S(\mathbf{G})$  drastically decreases, especially at  $t'/t \sim -0.3$ ,

and  $\mathbf{G}$  is no longer a characteristic wave number for  $|t'/t| \gtrsim -0.45$ . In Fig. 26(b), we compare the  $t'/t$  dependence of  $S(\mathbf{G})$  with that of  $P_d^\infty$ . When  $S(\mathbf{G})$  abruptly decreases for  $|t'/t| > 0.25$ ,  $P_d^\infty$  follows including the system size dependence. In Fig. 27, we show the  $U/t$  dependence of  $S(\mathbf{G})$ . Although in every case  $S(\mathbf{G})$  increases

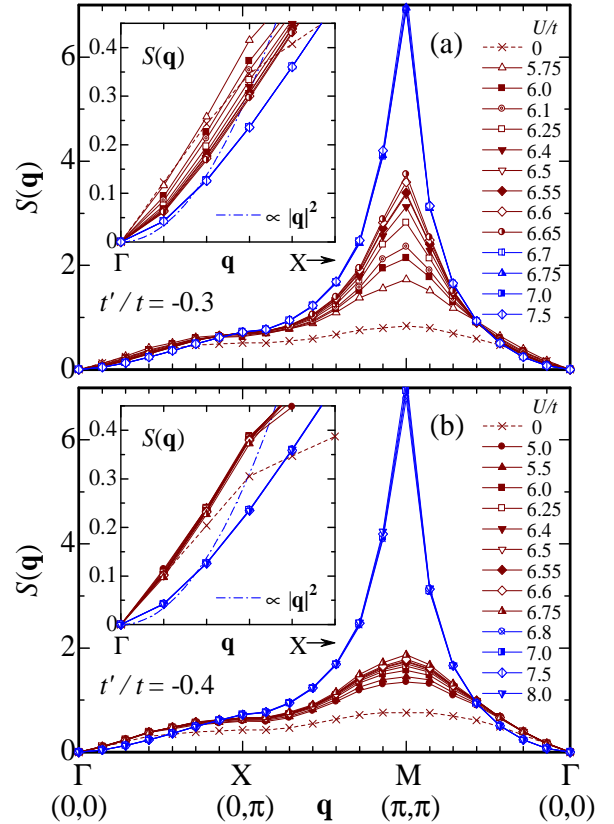


Fig. 25. (Color online) Spin structure factor for (a)  $t'/t = -0.3$  [ $U_c/t = 6.69$ ] and (b)  $t'/t = -0.4$  [ $U_c/t = 6.78$ ] for various  $U$  near  $U_c$  in  $\Psi_Q^d$ . The system size is of  $L = 14$ . Brown (blue) symbols and lines denote the data in conductive (insulating) regimes. The insets show the magnification of the region near the  $\Gamma$  point on the  $\Gamma$ -X line, and the symbols are common to the main panel. Data points of different  $U$ 's for  $U > U_c$  almost overlap one another. Similar data for  $t'/t = 0$  are given in Fig. 14.

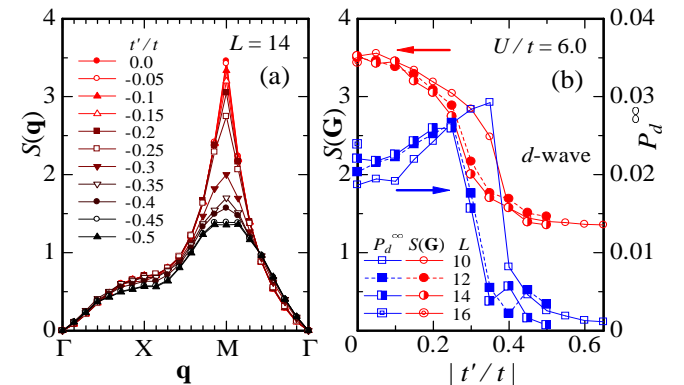


Fig. 26. (Color online) (a)  $t'/t$  dependence of spin structure factor for  $U/t = 6$ , where  $P_d^\infty$  is considerably enhanced especially for small  $t'/t$ . (b) Spin structure factor at the AF wave number  $\mathbf{G}$  for  $U/t = 6$  as a function of  $t'/t$  is denoted by red lines (left axis). Simultaneously, the  $d$ -wave pair correlation function is plotted with blue lines.

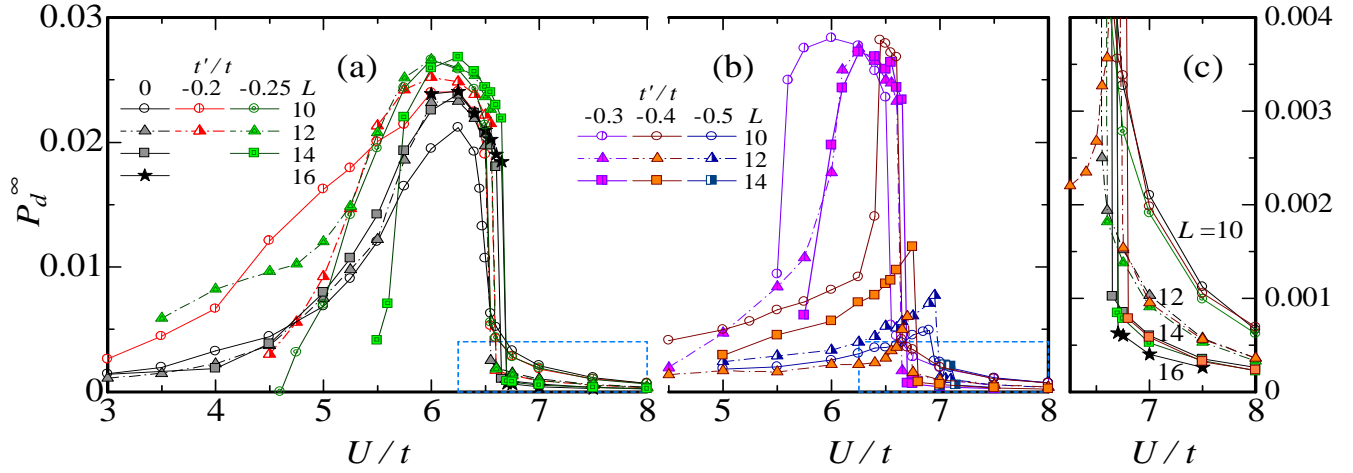


Fig. 24. (Color online) Large- $|r|$  value of the  $d$ -wave pair correlation function  $P_d(\mathbf{r})$  for (a) small  $|t'/t|$  ( $\leq 0.25$ ) and (b) large  $|t'/t|$  ( $\geq 0.3$ ). Data of some system sizes for each value of  $t'/t$  are plotted simultaneously. (c) Magnification of  $P_d^\infty$  near the Mott critical points. The data only for  $t'/t = 0, -0.25$  and  $-0.4$  are shown for clarity. The range of (c) is indicated by the light-blue boxes in (a) and (b).

more or less as  $U/t$  increases, the range of sizable increase [ $S(\mathbf{G}) \gtrsim 2$ ] in the conductive regime roughly corresponds to  $U_{\text{onset}} \lesssim U < U_c$ , and is accompanied by the marked increase of  $P_d^\infty$  (Fig. 24). We have confirmed for a wide range of model parameters that whenever  $P_d^\infty$  is appreciably enhanced,  $S(\mathbf{q})$  has an evident peak at  $\mathbf{q} = \mathbf{G}$ . These results strongly support the idea that the SC in this model is induced by the AF spin correlation. Incidentally, this mechanism is reflected in the ratio of energy components. As shown in Table III ( $U/t = 6.25$ ), when SC is weak ( $|t'/t| = 0.4$ ),  $\rho$  is only slightly smaller than the noninteracting value, whereas for robust SC ( $|t'/t| = 0.25$ ),  $\rho$  becomes less than half the value for  $U = 0$ ; the diagonal hopping is considerably suppressed.

Next, we take up the energy gain in the SC transition. Shown in Fig. 28 are the components of condensation energy, that is, the differences in kinetic and interaction energies between  $\Psi_Q^d$  and  $\Psi_Q^{\text{FS}}$ ; the concrete expression is given in the figure. Here,  $E_{\text{kin}} = \langle \mathcal{H}_{\text{kin}} \rangle = E_t + E_{t'}$ , and  $\Delta E_{\text{kin}} + \Delta E_U = \Delta E$  ( $\geq 0$ ) [eq.(20)]. In the SC regime ( $U < U_c$ ),  $\Delta E_{\text{int}}$  ( $\Delta E_{\text{kin}}$ ) is always positive (negative),

regardless of the value of  $t'/t$ . This indicates that the SC transition is induced by the gain in the interaction energy at the cost of kinetic energy. This feature smoothly continues to the weak-coupling limit ( $U/t \rightarrow 0$ ), and common to conventional BCS superconductors. Although the component of energy gain switches to the kinetic energy at  $U = 8t$ – $11t$ , which broadly corresponds to  $U_c^{\text{FS}}$ , yet SC is excluded for  $U > U_c$ . The kinetic-energy-driven SC is not realized at half filling, in contrast to the doped cases.<sup>8</sup>

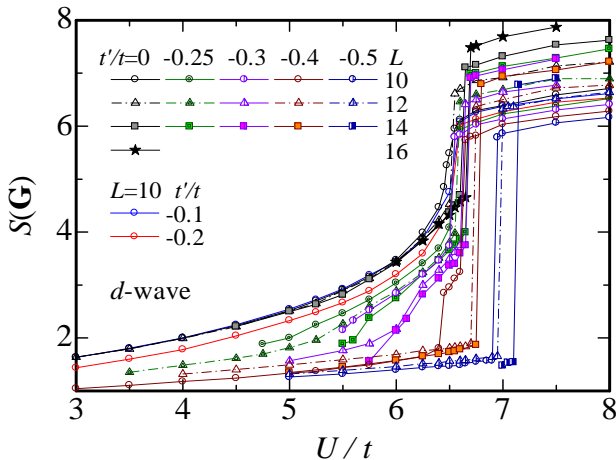


Fig. 27. (Color online)  $U/t$  dependence of spin structure factor at the AF wave number  $\mathbf{G}$  for various values of  $t'/t$  and  $L$ .

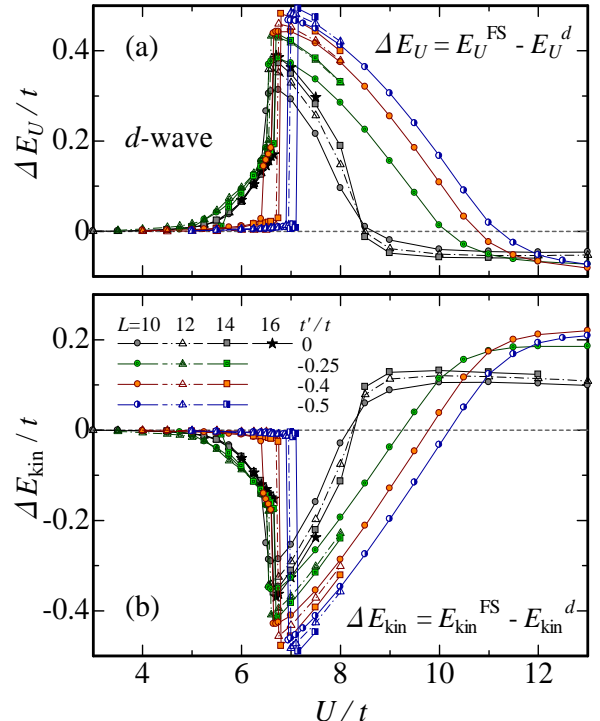


Fig. 28. (Color online) (a) Interaction and (b) kinetic components of the condensation energy due to  $\Psi_Q^d$  as a function of interaction strength for four values of  $t'/t$ . Some system sizes are simultaneously plotted. The symbols and the scales are common to both panels.

Incidentally, this behavior of  $\Delta E_{\text{kin}}$  and  $\Delta E_U$  is not restricted to the  $d$ -wave state, but found for some order-disorder transitions. As an example, we plot, in Fig. 29(b),  $\Delta E_{\text{kin}}$  ( $= \Delta E_t$ ) and  $\Delta E_U$  of the AF state  $\Psi_Q^{\text{AF}}$ , eq. (14), which will be discussed in the next section, for  $t'/t = 0$ . The interaction part  $\Delta E_U$  makes a positive contribution to  $\Delta E$  for  $U/t \lesssim 8$ , whereas the kinetic part  $\Delta E_t$  for  $U/t \gtrsim 7$ . Hence, the behavior is qualitatively identical to that of  $\Psi_Q^d$ . Such behavior is also observed in SC and CDW states for the two-dimensional attractive Hubbard model.<sup>65</sup>

## 6. Phase Diagram and Antiferromagnetism

To this point, we have not taken up the competition with an AF state, but it is a crucial problem to draw a phase diagram. We hence compare the stability between  $\Psi_Q^d$  and the AF ordered state  $\Psi_Q^{\text{AF}}$ , eq. (14), into which we do not introduce band renormalization parameters, to equalize the condition with  $\Psi_Q^d$ . Whenever  $\Delta_{\text{AF}}$  is finite at half filling,  $\Psi_Q^{\text{AF}}$  is insulating and has an AF long-range order; the sublattice magnetization  $m$  [eq. (19)] behaves similarly to  $\Delta_{\text{AF}}$ .

In Fig. 30, we show a phase diagram constructed as follows. The boundary between AF-I and P-M ( $|t'/t| \leq 0.2$ ) is determined by the points where the extrapolated values of  $\Delta_{\text{AF}}$  vanish; the boundary between AF-I and SC (or P-I) by the comparison of the total energies; the boundary between P-I and P-M by  $U_c/t$  for the largest systems for each  $t'/t$  obtained in §3. The last boundary are extended to  $t'/t = 0$  if  $\Psi_Q^{\text{AF}}$  is not allowed, as indicated by a dashed line. It is insignificant to fix the boundary between SC and P-M, because small magnitude of  $\Delta$  often survives for extremely small  $U/t$ ; instead, we show  $U_{\text{onset}}/t$  with a dashed line.

For  $t'/t = 0$ , a continuous metal-to-AF-insulator transition will take place at  $U = U_c^{\text{AF}} = 0$ ,<sup>14</sup> due to the complete nesting condition. This AF state is very stable and continues to the Heisenberg limit ( $U/t \rightarrow \infty$ ). Our result is consistent with it, as shown in Fig. 29(a), where the condensation energy for  $\Psi_Q^{\text{AF}}$  is always larger than that of  $\Psi_Q^d$ . The nature of the continuous transi-

tion seems to be preserved in the region of small  $|t'/t|$ , although  $U_c^{\text{AF}}$  becomes finite, and the tendency toward a first-order transition gradually develops, as  $|t'/t|$  increases. Note that, as the frustration becomes strong,  $\Psi_Q^{\text{AF}}$  is rapidly destabilized, and surrenders to  $\Psi_Q^d$  at  $t' = t'_c \sim -0.2t$ . Moreover,  $|t'_c/t|$  tends to decrease as  $U/t$  increases; this feature is consistent with the result that the AF state has the largest range of  $n$  at  $U \sim W$  in a phase diagram in the  $n$ - $U$  plane.<sup>8</sup> However, this tendency does not accord with the arguments in the  $J$ - $J'$  spin model, which is an effective model of eq. (1) for large  $U/t$ . Various studies of the  $J$ - $J'$  model<sup>66</sup> concluded that the AF order vanishes at rather large values  $J'/J \sim 0.4$  ( $|t'/t| \sim 0.63$ ).

We consider that this discrepancy is primarily due to the choice of variational states: (1)  $\Psi_Q^d$  does not have a seed of AF long-range order, although the AF short-range correlation appreciably develops, and (2) in  $\Psi_Q^{\text{AF}}$ , we have not allow for the band renormalization effect. These two requirements are satisfied simultaneously by adopting a coexisting state of AF and SC gaps,<sup>67, 68</sup> with a band renormalization effect.<sup>46</sup> In fact, we have performed VMC calculations using such a wave function for the anisotropic triangular lattice, and found that the area of the AF phase enormously expands.<sup>69</sup> A similar result has been obtained independently by Chen,<sup>70</sup> and also for the checkerboard lattice by Koga *et al.*<sup>41</sup> Thus, it is urgent to improve the wave function in this line to refine the phase diagram.

## 7. Conclusions

### 7.1 Summary

Using an optimization variational Monte Carlo method, we have studied the half-filled-band Hubbard model on frustrated square lattices, eq. (1). Our primary aim is to understand the mechanisms of the Mott transition and of the  $d_{x^2-y^2}$ -wave SC arising in the Hubbard model. To this end, we introduce an intersite correlation factor that controls the binding between a doublon and a holon into the trial functions—normal (Fermi sea),

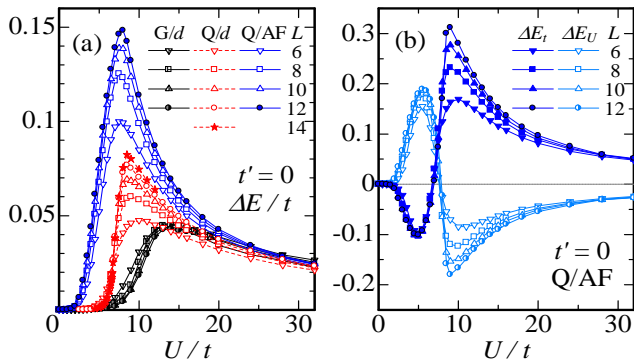


Fig. 29. (Color online) (a) Comparison of the condensation energy for  $t'/t = 0$  among  $\Psi_Q^d$  (indicated by  $Q/d$ ),  $\Psi_Q^{\text{AF}}$  ( $Q/\text{AF}$ ) and  $\mathcal{P}_G\Phi_d$  ( $G/d$ ), for which  $\Delta E = E(\mathcal{P}_G\Phi_{\text{FS}}) - E(\mathcal{P}_G\Phi_d)$ . Several system sizes are plotted to see the  $L$  dependence. (b) Kinetic (closed symbols) and interaction (open symbols) parts of the condensation energy due to  $\Psi_Q^{\text{AF}}$  for  $t'/t = 0$ . Four system sizes are used.

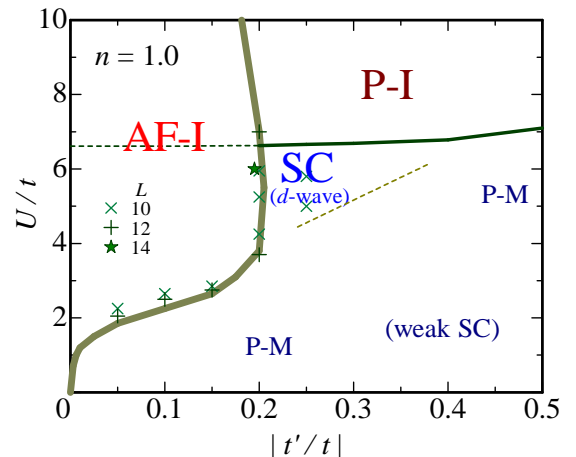


Fig. 30. (Color online) Ground-state phase diagram in the  $t'$ - $U$  space constructed from the VMC calculations performed in this work. The abbreviation AF-I, P-I (P-M) and SC denotes AF insulator, paramagnetic insulator (metal) and superconductor, respectively.

$d$ -wave singlet and AF states—. We have succeeded in describing the  $d$ -wave SC and a Mott transition simultaneously in a sole approach. We itemize our main findings:

(1) Within the  $d$ -wave singlet state, a first-order Mott (conductor-to-nonmagnetic insulator) transition takes place at  $U_c$  approximately of the bandwidth for arbitrary  $t'/t$ . In the insulating regime, most doublon-holon pairs are actually confined within the nearest-neighbor sites, in contrast to in the conductive regime. The critical  $U_c/t$  gradually increases as the frustration becomes strong. This transition is not directly related to a magnetic order.

(2) We have confirmed that also in the projected Fermi sea, a first-order Mott transition without relevance to magnetism arises at somewhat larger  $U/t$  than the bandwidth for arbitrary  $t'/t$ , although the state does not have the lowest energy.

(3) The nonmagnetic insulating state ( $d$ -wave singlet state for  $U > U_c$ ) has a considerably low energy and a strong short-range AF correlation. According to the small- $|\mathbf{q}|$  behavior of  $S(\mathbf{q})$ , the  $d$ -wave state tends to have short singlet bonds due to the nearest-neighbor pairing eq. (12), in contrast to the projected Fermi sea, which clearly does not have a spin gap.

(4) Robust SC with the  $d_{x^2-y^2}$ -wave symmetry appears for moderate values of  $U/t$  ( $\sim 6$ ) and  $t'/t$  ( $0.2 \lesssim |t'/t| \lesssim 0.35$ ). This area is adjacent to both domains of a Mott insulator and an AF long-range order. The phase diagram obtained in this study is shown in Fig. 30.

(5) By comparing the pair correlation function with  $S(\mathbf{q})$ , it is found that robust SC is always accompanied by appreciably enhanced short-range AF spin correlation, which is weakened by the frustration and almost vanishes for  $|t'/t| \gtrsim 0.35$ . The SC transition is induced by the gain in interaction energy; this mechanism is identical to that in the weak correlation limit as well as that of conventional BCS superconductors.

(6) The AF long-range order prevailing in the weakly frustrated cases ( $|t'/t| \lesssim 0.2$ ) is rapidly destabilized as  $|t'/t|$  increases, if a band renormalization effect is not introduced.

## 7.2 Further discussions

(1) In comparing the present study for the frustrated square lattice [Fig. 1(a)] with the preceding study,<sup>6</sup> in which almost the same wave functions are applied to the anisotropic triangular lattice [Fig. 1(b)], the results for the two lattices are qualitatively identical, indicating the effect of frustration works similarly, unless  $|t'/t|$  is too large. However, the critical values with respect to  $t'/t$  are broadly doubled for the latter lattice, namely, the AF state becomes unstable approximately at  $|t'/t| = 0.2$  for the former and 0.4 for the latter, and the robust SC disappears approximately at  $|t'/t| = 0.35$  for the former, and 0.8 for the latter. This can be explained by the difference in the number of frustrated bonds.

(2) Recently, using a VMC method with two-body long-range Jastrow factor for the square lattice ( $t' = 0$ ), Capello *et al.*<sup>71</sup> found that a metal-to-insulator transition arises, similar to that in  $\Psi_Q^{\text{FS}}$ , for example, in the behavior of  $Z$  and  $d$ . The critical value of their function

is  $U_c/t \sim 8.5$ , which resembles 8.73 ( $L = 18$ ) in  $\Psi_Q^{\text{FS}}$ . Although their transition is regarded as continuous, evidence of the first order will be found by a detailed analysis for larger systems. In their wave function, an explicit (four-body) doublon-holon binding factor is not introduced, but a short-range part of the two-body Jastrow factor will substantially work as a binding factor under the condition of strong electron repulsion at half filling. It is interesting to reveal the relation between the two wave functions.

(3) In this paper, we have restricted the electron density to half filling ( $n = 1$ ). When carriers are doped, unless the doping rate  $|1 - n|$  is too large, the doublon-holon-binding effect remains significant, as we showed for  $t' = 0$  in the previous letter.<sup>8</sup> The Mott transition at half filling changes to a crossover from weakly- to strongly-correlated regimes. As  $|1 - n|$  increases, the AF order is rapidly destabilized, and the SC phase expands to the region of large  $U/t$ , in consistent with the behavior of high- $T_c$  cuprates. We will report detailed description of doped cases with the effect of frustration elsewhere.

## Acknowledgments

We would like to thank Kenji Kobayashi and Tsutomu Watanabe for useful discussions. We appreciate the beneficial communication with Y. C. Chen on the stability of the AF state. This work is partly supported by Grant-in-Aids from the Ministry of Education, Culture, Sports, Science and Technology, and by the Supercomputer Center, ISSP, University of Tokyo.

- 1) K. Kanoda: *Physica C* **282-287** (1997) 299; K. Miyagawa, K. Kanoda and A. Kawamoto: *Chem. Rev.* **104** (2004) 5635; R. H. McKenzie: *Science* **278** (1997) 820.
- 2) H. Kino and H. Fukuyama: *J. Phys. Soc. Jpn.* **65** (1996) 2158.
- 3) A. Tsukada, Y. Krockenberger, M. Noda, H. Yamamoto, D. Manske, L. Alff and M. Naito: *Solid State Commun.* **133** (2005) 427.
- 4) C. J. Umrigar, K. G. Wilson and J. W. Wilkins: *Phys. Rev. Lett.* **60** (1988) 1719.
- 5) For instance, C. J. Umrigar and C. Filippi: *Phys. Rev. Lett.* **94** (2005) 150201; S. Sorella: *Phys. Rev. B* **71** (2005) 241103.
- 6) T. Watanabe, H. Yokoyama, Y. Tanaka and J. Inoue: *J. Phys. Soc. Jpn.* **75** (2006) 074707.
- 7) B. Bernu, P. Lecheminant, C. Lhuillier and L. Pierre: *Phys. Rev. B* **50** (1994) 10048; L. Capriotti, A. E. Trumper and S. Sorella: *Phys. Rev. Lett.* **82** (1999) 3899.
- 8) H. Yokoyama, Y. Tanaka, M. Ogata and H. Tsuchiura: *J. Phys. Soc. Jpn.* **73** (2004) 1119.
- 9) J. Hubbard: *Proc. Roy. Soc.* **A276** (1963) 237.
- 10) J. Kanamori: *Prog. Theor. Phys.* **30** (1963) 275.
- 11) M. C. Gutzwiller: *Phys. Rev. Lett.* **10** (1963) 159.
- 12) P. W. Anderson: *Science* **235** (1987) 1196.
- 13) For instance, T. Tanamoto, H. Kohno and H. Fukuyama: *J. Phys. Soc. Jpn.* **61** (1992) 1886; T. Tohyama and S. Maekawa: *Phys. Rev. B* **49** (1994) 3596; R. Raimondi, J. H. Jefferson and L. F. Feiner: *Phys. Rev. B* **53** (1996) 8774; E. Pavarini, I. Dasgupta, T. Saha-Dasgupta, O. Jepsen and O. K. Anderson: *Phys. Rev. Lett.* **87** (2001) 047003.
- 14) For instance, J. E. Hirsch: *Phys. Rev. B* **31** (1985) 4403.
- 15) H. Kondo and T. Moriya: *J. Phys. Soc. Jpn.* **65** (1996) 2559, *J. Phys. Soc. Jpn.* **67** (1998) 234.
- 16) R. Chitra and G. Kotliar: *Phys. Rev. Lett.* **83** (1999) 2386; T. Pruschke: *Prog. Theor. Phys.* **160** (2005) 274.
- 17) T. Kashima and M. Imada: *J. Phys. Soc. Jpn.* **70** (2001) 3052.
- 18) T. Mizusaki and M. Imada: *cond-mat/0604389*.

- 19) For instance, B. Kyung and A. -M. S. Tremblay: cond-mat/0604377, and references therein.
- 20) R. Jastrow: Phys. Rev. **98** (1955) 1479.
- 21) M. C. Gutzwiller: Phys. Rev. **137** (1965) A1726.
- 22) For a review, D. Vollhardt: Rev. Mod. Phys. **56** (1984) 99.
- 23) W. L. McMillan: Phys. Rev. **138** (1965) A442; D. Ceperley, G. V. Chester and K. H. Kalos: Phys. Rev. B **16** (1977) 3081.
- 24) H. Yokoyama and H. Shiba: J. Phys. Soc. Jpn. **56** (1987) 1490.
- 25) C. Gros, R. Joynt and T. M. Rice, Phys. Rev. B **36** (1987) 381.
- 26) W. Metzner and D. Vollhardt: Phys. Rev. B **37** (1988) 7382; F. Gebhard and D. Vollhardt: Phys. Rev. B **38** (1988) 6911.
- 27) H. Yokoyama and H. Shiba: J. Phys. Soc. Jpn. **59** (1990) 3669.
- 28) C. Castellani, C. Di Castro, D. Feinberg and J. Ranninger: Phys. Rev. Lett. **43** (1979) 1957.
- 29) T. A. Kaplan, P. Horsch and P. Fulde, Phys. Rev. Lett. **49** (1982) 889; see also P. Fazekas, Physica Scripta T **29** (1989) 125.
- 30) E. H. Lieb and F. Y. Wu: Phys. Rev. Lett. **21** (1968) 192.
- 31) H. Yokoyama and M. Ogata: Phys. Rev. Lett. **67** (1991) 3610; Phys. Rev. B **53** (1996) 5758.
- 32) H. Yokoyama and H. Shiba: J. Phys. Soc. Jpn. **57** (1988) 2482.
- 33) C. Gros: Ann. Phys. (New York) **189** (1989) 53.
- 34) H. Yokoyama and M. Ogata: J. Phys. Soc. Jpn. **65** (1996) 3615.
- 35) Here,  $S$  is explicitly given by

$$\sum_{(ij)\sigma} \frac{-it}{U} \left[ n_{i-\sigma}(1-n_{j-\sigma})c_{i\sigma}^\dagger c_{j\sigma} - n_{j-\sigma}(1-n_{i-\sigma})c_{i\sigma}^\dagger c_{j\sigma} \right].$$

For sufficiently large  $U/t$  and  $n \sim 1$ , one may expand  $e^{iS}$ , and keep only essential ( $t$ - $J$ ) terms of the order  $t^2/U$ , in addition to the zeroth-order terms. See, A. B. Harris and R. V. Lange, Phys. Rev. **157** (1967) 295.

- 36) H. Otsuka: J. Phys. Soc. Jpn. **61** (1992) 1645.
- 37) A. J. Millis and S. N. Coppersmith: Phys. Rev. B **43** (1991) 13770.
- 38) H. Yokoyama: Prog. Theor. Phys. **108** (2002) 59.
- 39) In the results of ref. 27,  $\Psi_q^{\text{FS}}$ , even in one dimension, seems to induce a Mott transition between  $U/t = 4$  and 16. We speculate that a longer-range doublon-holon binding factor is crucial in one dimension to reduce  $U_c$  down to zero.
- 40) S. Kuratani, A. Koga and N. Kawakami: private communication.
- 41) A. Koga, T. Yoshioka, N. Kawakami and H. Yokoyama: submitted to J. Mag. Mag. Mat. and Physica C.
- 42) A. Koga, N. Kawakami, H. Yokoyama and K. Kobayashi: to appear in the proceedings of LT24.
- 43) J. P. Bouchaud, A. Georges and C. Lhuillier: J. Phys. (Paris) **49** (1988) 553.
- 44) H. Yoshimura and D. S. Hirashima: J. Phys. Soc. Jpn. **74** (2005) 712; T. Watanabe, T. Miyata, H. Yokoyama, Y. Tanaka and J. Inoue: J. Phys. Soc. Jpn. **74** (2005) 1942.
- 45) F. C. Zhang, C. Gros, T. M. Rice and H. Shiba: Supercond. Sci. Tech. **1** (1988) 36.
- 46) A. Himeda and M. Ogata: Phys. Rev. Lett. **85** (2000) 4345.
- 47) H. Shiba: Prog. Theor. Phys. **48** (1972) 2171; Y. Nagaoka: Prog. Theor. Phys. **52** (1974) 1716.
- 48) H. Yokoyama and H. Shiba: J. Phys. Soc. Jpn. **67** (1987) 3582.
- 49) For instance, K. Kobayashi and K. Iguchi: Phys. Rev. B **47** (1993) 1775.
- 50) W. H. Press, S. A. Teukolsky, W. T. Vetterling and B. P. Flannery: *Numerical Recipes in FORTRAN, second ed.* (Cambridge, New York, 1992) p.406.
- 51) In the present VMC procedure, if the energy barrier between the two local energy minima is sufficiently high, the optimized variational parameters are trapped in the local minima to which the initial parameter values tend. Thus, as seen in Figs. 3, 5 and 6, we can obtain the optimized values for both local minima by giving the respective initial parameters

anticipated from those obtained for nearby data points. On the other hand, if the barrier becomes as low as the statistical fluctuation in  $E/t$  (we assume there are still two energy

minima), the parameters readily arrive at the global minima, jumping over the barrier. Therefore, it is not easy to determine the values of  $U/t$  at which the double-minimum structure of  $E/t$  vanishes, namely, to draw the accurate hysteresis curves.

- 52) The data of  $\mu$  for  $L = 8$ -16 seems fitted well with a linear function of  $N_s^{-1}$  ( $= L^{-2}$ ). Thereby, we have estimated approximate values of  $\mu$  for  $L = \infty$  and  $t' = 0$ , as  $\mu = 0.912$ - $0.945$  for  $U/t = 6.75$ - $10$ ; as  $U/t$  increases,  $\mu$  tends to increase.
- 53) W. F. Brinkman and T. M. Rice: Phys. Rev. B **2** (1970) 4302.
- 54) M. J. Rozenberg, R. Chitra and G. Kotliar: Phys. Rev. Lett. **83** (1999) 3498.
- 55) The behavior of  $n(\mathbf{k})$  for the finite values of  $t'/t$  is basically the same. In some cases, however, the position of the (quasi) Fermi surface moves as  $U/t$  increases and crosses a discrete  $\mathbf{k}$ -point of the finite system. Then, it becomes difficult to determine the proper values of  $Z$  as a function of  $U/t$ , because the position of the Fermi surface is not specified. For instance, the case of  $t'/t = -0.25$  and  $L = 14$  exhibits such inconvenient behavior.
- 56) In ref. 6, the optimized chemical potential  $\zeta$  is positive, because the sign of  $t'/t$  is assumed positive, contrary to the present case. The behavior of  $|\zeta|$  for  $U < U_c$  in ref. 6 is broadly similar to that in Fig. 4(e), whereas, for  $U > U_c$ ,  $\zeta$  decreases only to nearly zero, which is the value for  $t'/t = 0$ .
- 57) R. Bulla: Phys. Rev. Lett. **83** (1999) 136.
- 58) Y. Shimizu, K. Miyagawa, K. Kanoda, M. Maesato and G. Saito: Phys. Rev. Lett. **91** (2003) 107001.
- 59) For  $6.4 \lesssim U/t < 6.64$  ( $= U_c/t$ ),  $\Psi_Q^d$  with  $t'/t = -0.4$  and  $L = 10$  takes a special  $\mathbf{k}$ -point configuration [observed in  $n(\mathbf{k})$  (not shown)], which is different from the cases of  $U/t \leq 6.4$ , and is advantageous to SC. One find in Fig. 4 that each of the optimized parameters for  $t'/t = -0.4$  and  $L = 10$  has a value similar to that which brings about SC (e.g.  $|t'/t| \leq 0.3$ ) only for  $6.4 \lesssim U/t < 6.64$ . Correspondingly,  $P_d(\mathbf{r})$  shown in Fig. 24(b) has extraordinary large values for the above values of  $U/t$ . This enhancement of SC is spurious, because there are no such remarkable behavior for  $L = 12$  and 14. Such behavior sometimes appears near the critical value of  $t'/t$ , where dominant SC vanishes, and for specific system sizes, boundary conditions and model parameters. Also in this point, we need to check the system-size dependence.
- 60) When  $U/t$  is small and the coherence length is long, one needs to consider SC correlation functions of longer Cooper pairs. In the present study, however,  $P_d(\mathbf{r})$  in eq. (21) is useful, because we are interested in the SC arising, particularly, near the Mott transition.
- 61) As  $L$  is increased, the magnitude of spikes gradually decreases. We need the systems of  $L = 30$ -50 in which the spikes for  $U/t = 0$  look negligible in the scale of Fig. 23.
- 62) C. T. Shih, T. K. Lee, R. Eder, C. -Y. Mou and Y. C. Chen: Phys. Rev. Lett. **92** (2004) 227002.
- 63) We adopt the Manhattan metric to measure  $|\mathbf{R}|$  and  $|\mathbf{r}|$ .
- 64) S. Onari, H. Yokoyama and Y. Tanaka: in preparation.
- 65) H. Yokoyama: unpublished.
- 66) L. Spanu and A. Parola: Phys. Rev. B **72** (2005) 174418; L. Capriotti and S. Sorella: Phys. Rev. Lett. **84** (2000) 3173; J. Oitmaa and W. Zheng: Phys. Rev. B **54** (1996) 3022; J. Igarashi: J. Phys. Soc. Jpn. **62** (1993) 4449; T. Nakamura and N. Hatano: J. Phys. Soc. Jpn. **62** (1993) 3062; J. H. Xu and C. S. Ting: Phys. Rev. B **42** (1990) 6861.
- 67) T. Giamarchi and C. Lhuillier: Phys. Rev. B **43** (1991) 12943.
- 68) A. Himeda and M. Ogata: Phys. Rev. B **60** (1999) 9935.
- 69) T. Watanabe, H. Yokoyama, Y. Tanaka and J. Inoue: submitted to J. Mag. Mag. Mat., and in preparation.
- 70) Y. C. Chen: private communication.
- 71) M. Capello, F. Becca, S. Yunoki and S. Sorella: Phys. Rev. B **73** (2006) 245116.